

**Synthesis and Characterization of Rare Earth Metals Substituted
Barium Hexaferrite Nanoparticles for Microwave Absorption
Applications**



By

Abdur Rehman Khan Niazi

(Registration No: 00000429819)

Department of Materials Engineering

School of Chemical and Materials Engineering

National University of Sciences & Technology (NUST)

Islamabad, Pakistan

(2024)

**Synthesis and Characterization of Rare Earth Metals Substituted
Barium Hexaferrite Nanoparticles for Microwave Absorption
Applications**



By

Abdur Rehman Khan Niazi

(Registration No: 00000429819)

A thesis submitted to the National University of Sciences and Technology, Islamabad,

in partial fulfillment of the requirements for the degree of

Master of Science in
Nanoscience and Engineering

Supervisor: Dr. Iftikhar Hussain Gul

School of Chemical and Materials Engineering

National University of Sciences & Technology (NUST)

Islamabad, Pakistan


(2024)

THESIS ACCEPTANCE CERTIFICATE



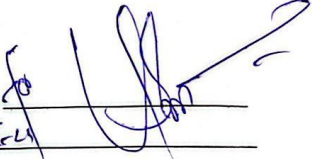
THESIS ACCEPTANCE CERTIFICATE

Certified that final copy of MS thesis written by Mr Abdur Rehman Khan Niazi (Registration No 00000429819), of School of Chemical & Materials Engineering (SCME) has been vetted by undersigned, found complete in all respects as per NUST Statues/Regulations, is free of plagiarism, errors, and mistakes and is accepted as partial fulfillment for award of MS degree. It is further certified that necessary amendments as pointed out by GEC members of the scholar have also been incorporated in the said thesis.

Signature: 

Name of Supervisor: Dr Iftikhar Hussian Gul

Date: 26/09/2024

Signature (HoD): 

Date: 26/09/24

Signature (Dean/Principal): 

Date: 26/9/24

TH - 1

NSE-16-2022

Form TH-1

National University of Sciences & Technology (NUST) MASTER'S THESIS WORK


Formulation of Guidance and Examination Committee (GEC)

Name: Abdur Rehman Khan Niazi NUST Reg No: 00000429819
 Department: Department of Materials Engineering Specialization: Master of Science in Nanoscience and Engineering
 Credit Hour Completed: 24.0 CGPA: 3.63

Course Work Completed

S/No:	Code:	Title:	Core/Elective:	CH:	Grade:
1.	NSE-813	Essentials of Nanoscience and Engineering	Compulsory	3.0	C+
2.	EME-812	Detection And Analysis Of Explosives	Elective	3.0	A
3.	EME-800	Science Of Energetic Materials	Elective	3.0	A
4.	MSE-856	Nano Material and Processing	Compulsory	3.0	B+
5.	EME-805	Explosives Manufacture, Formulation And Filling	Elective	3.0	A
6.	EME-802	Advanced Energetic Materials	Elective	3.0	B+
7.	RM-898	Research Methodology	Additional	2.0	Q
8.	MSE-854	Characterization Of Materials	Compulsory	3.0	A
9.	NSE-845	Nanolithography And Device Fabrication	Elective	3.0	B+

Date: 27-Feb-2024

Student's Signature: 

Thesis Committee


- Name: Iftikhar Hussain Gul (Supervisor)
Department: Department of Materials Engineering
- Name: Nasir Mahmood Ahmad (Internal)
Department: Department of Materials Engineering
- Name: Usman Liaqat (Internal)
Department: Department of Materials Engineering

Signature: 

Signature: 


Signature: 

Date: 27-Feb-2024

Signature of Head of Department: 

APPROVAL

Date: 27-Feb-2024

Signature of Dean/Principal: 

School of Chemical & Materials Engineering (SCME) H-12 Campus,

TH - 4



National University of Sciences & Technology (NUST)

FORM TH-4

MASTER'S THESIS WORK

We hereby recommend that the dissertation prepared under our supervision by

Regn No & Name: 00000429819 Abdur Rehman Khan Niazi

Title: Synthesis and Characterization of Rare Earth Metals Substituted Barium Hexaferrite Nanoparticles for Microwave Absorption Applications.

Presented on: 18 Sep 2024 at: 1430 hrs in SCME Seminar Hall

Be accepted in partial fulfillment of the requirements for the award of Masters of Science degree in Nanoscience & Engineering.

Guidance & Examination Committee Members

Name: Dr Zakir Hussain

Signature: [Signature]

Name: Dr Usman Liaqat

Signature: [Signature]

Supervisor's Name: Dr Iftikhar Hussain Gul

Signature: [Signature]

Dated: 18/09/2024

[Signature]
Head of Department

Date 24/9/24

[Signature]
Dean/Principal

Date 26/9/24

School of Chemical & Materials Engineering (SCME)

AUTHOR'S DECLARATION

I Abdur Rehman Khan Niazi hereby state that my MS thesis titled "Synthesis and Characterization of Rare Earth Metals Substituted Barium Hexaferrite Nanoparticles for Microwave Absorption Applications" is my own work and has not been submitted previously by me for taking any degree from National University of Sciences and Technology, Islamabad or anywhere else in the country/ world.

At any time if my statement is found to be incorrect even after I graduate, the University has the right to withdraw my MS degree.

Name of Student: Abdur Rehman Khan Niazi

Date: 28 August 2024

PLAGIARISM UNDERTAKING

I solemnly declare that research work presented in the thesis titled “Synthesis And Characterization of Rare Earth Metals Substituted Barium Hexaferrite Nanoparticles for Microwave Absorption Applications” is solely my research work with no significant contribution from any other person. Small contribution/ help wherever taken has been duly acknowledged and that complete thesis has been written by me.

I understand the zero-tolerance policy of the HEC and National University of Sciences and Technology (NUST), Islamabad towards plagiarism. Therefore, I as an author of the above titled thesis declare that no portion of my thesis has been plagiarized and any material used as reference is properly referred/cited.

I undertake that if I am found guilty of any formal plagiarism in the above titled thesis even after award of MS degree, the University reserves the rights to withdraw/revoke my MS degree and that HEC and NUST, Islamabad has the right to publish my name on the HEC/University website on which names of students are placed who submitted plagiarized thesis.

Student Signature:  _____

Name: Abdur Rehman Khan Niazi

DEDICATION

"To my Grand Father, who is no longer with me to witness me complete my work. May I have the same unwavering dedication to my field in science that you had in me."

ACKNOWLEDGEMENTS

Allah has been kind and merciful, for guiding me throughout my academic journey. I would like to express my deepest gratitude to spiritual Great Grand Father, my Grand Father, my mother **Fateh Khatoon**, my father **Saif Ullah Khan**, my brother **Abdullah Khan**, my sister **Sehrish Khan** and wife **Shumaila Noreen**, who have been my constant source of support and inspiration. Their unwavering belief in me has been a driving force behind my success, and I am forever grateful for their love and support.

I am deeply thankful to **Dr. Iftikhar Hussain Gul** for his guidance, support, and unwavering commitment throughout this research. His mentorship has been invaluable in shaping the direction of this work, and I am grateful for the opportunities he has provided for my academic growth.

I extend my appreciation to my committee members, **Dr. Zakir Hussain**, and **Dr. Usman Liaqat** for their insightful feedback, constructive criticism, and dedication to improving the quality of my work. Your expertise and diverse perspectives have enriched the content and methodology of this study.

I want to acknowledge the support and help provided by Ph.D. scholar **Mr. Muhammad Zarrar Khan**, Lab Engineer **Mr. Hamza-ul-Haq**, Lab Engineer **Mr. Muhammad Zafar Khan**, Lab Engineer **Mr. Muzammil**, **Mr. Marghoob Ahmed**, **Mr. Muhammad Arslan**, **Mr. Ammar Ud Din**, **Mr. Altaf Hussain**, **Mr. Anees Muhammad** and **Mr. Peer Muhammad** specially for the moral support provided by these all.

Abdur Rehman Khan Niazi

TABLE OF CONTENTS

ACKNOWLEDGEMENTS	IX
TABLE OF CONTENTS	X
LIST OF TABLES	XIII
LIST OF FIGURES	XIV
LIST OF SYMBOLS, ABBREVIATIONS AND ACRONYMS	XVI
ABSTRACT	XVIII
CHAPTER 1: INTRODUCTION	1
1.1 Background	1
1.2 Microwaves	1
1.2.1 Microwave Absorption	2
1.2.2 Microwave Absorbing Materials	3
1.2.3 Properties Affecting Microwave Absor	3
1.2.4 Magnetic Properties	3
1.2.5 Complex Permittivity & Permeability	4
1.2.6 Eddy Current Loss	4
1.2.7 Reflection Loss	5
1.2.8 Impedance Matching	5
1.2.9 Attenuation Constant	6
1.3 Introduction to Magnetism	6
1.3.1 Magnetism and its Types	6
1.3.2 Paramagnetic	7
1.3.3 Diamagnetic:	7
1.3.4 Ferromagnetism	7
1.3.5 Ferrimagnetism	8
1.3.6 Anti ferromagnetism	9
1.3.7 Super paramagnetic	9
1.4 History of Ferrites	10
1.4.1 Ferrites	10
1.4.2 Soft Ferrites	11
1.4.3 Hard Ferrites	11
1.4.4 Structural Classification of Ferrites	11
1.4.5 Spinel Ferrites	11
1.4.6 Garnet Ferrites	12
1.4.7 Ortho Ferrites	12
1.4.8 Hexagonal Ferrites	12
1.5 Hexaferrites	12
1.5.1 Classification of Hexaferrites	12

1.5.2	M-Type Hexaferrites	13
1.5.3	R-type Hexaferrites	13
1.5.4	X-type Hexaferrites	13
1.5.5	W-type Hexaferrites	14
1.5.6	Y-type Hexaferrites	14
1.5.7	Z-type Hexaferrites	14
1.5.8	Properties of Hexaferrites	14
1.5.9	Physical Properties	14
1.5.10	Magnetic Properties	15
1.5.11	Dielectric Properties	16
1.5.12	Synthesis Method of Hexaferrites	16
1.5.13	Applications of Hexaferrites	18
1.6	M-type Barium Hexaferrites	20
1.7	Thesis Scope	20
1.8	Research Objectives	21
CHAPTER 2: LITERATURE REVIEW		22
2.1	Barium based Hexaferrites. (BaM)	22
2.2	Literature Study	22
CHAPTER 3: MATERIALS AND METHODS		25
3.1	Materials Used	25
3.2	Synthesis of Lanthanum-Yttrium Substituted BaFe₁₂O₁₉	25
3.3	Laboratory Equipment & Accessories Used	26
3.4	Materials - BaY_xLa_xFe_{12-2x}O₁₉; (0.00 ≤ x ≤ 0.050)	26
3.1	Experimental Work	28
3.5	Sample Preparations for Characterization Techniques	29
3.5.1	Preparation of XRD Samples	30
3.5.2	Preparation of FTIR Samples	31
3.5.3	Preparation of SEM Samples	31
3.5.4	Preparation of VSM Samples	32
3.5.5	Preparation of VNA Samples	33
CHAPTER 4: RESULTS AND DISCUSSION		35
4.1	Structural Analysis (XRD)	35
4.2	SEM Analysis (Surface Morphological)	38
4.3	FTIR Analysis	40
4.3.1	Vibrational Modes and Permittivity	40
4.3.2	Enhanced Microwave Absorption	40
Composition(x)		42
Band Position (cm⁻¹)		42
v₁	42	
(Tetrahedral)		42
v₂	42	
(Octahedral)		42
v₃	42	
(Tetrahedral)		42

x = 0.00	42
582.23	42
540.92	42
430.65	42
x = 0.020	42
583.94	42
541.75	42
428.15	42
x = 0.035	42
582.76	42
542.10	42
429.47	42
x = 0.050	42
581.75	42
541.57	42
428.81	42
4.4 Magnetic Hysteresis	42
4.5 Microwave Absorption	46
4.5.1 Complex Permittivity and Complex Permeability	46
4.5.2 Dielectric Loss Tangent	50
4.5.3 Magnetic Loss Tangent	51
4.5.4 Impedence Matching and Reflection Loss	52
CHAPTER 5: CONCLUSIONS AND FUTURE RECOMMENDATION	57
5.1 Conclusion	57
5.2 Future Recommendation	58

LIST OF TABLES

Table 1.1: Physical properties of the main hexaferrites at ambient temperature	15
Table 3.1: Detail of Chemicals employed in the synthesis process	27
Table 3.2: Mass of the chemicals used for syntheses of BaY_xLa_xFe_{12-2x}O₁₉ as per their stoichiometric ratio.....	27
Table 4.1: Crystallite size (<i>D_c</i>), lattice parameters (<i>a = b, c</i>), ratio (<i>c/a</i>), d-spacing (<i>dhkl</i>) unit cell volume (<i>V_{cell}</i>), bulk density (<i>ρ_B</i>), x-ray density (<i>ρ_X</i>) and porosity (<i>P%</i>) of the synthesized samples.	36
Table 4.2: Represents the band positions for an octahedral and two tetrahedral (Fe-O and Me-O) vibrational modes of the synthesized samples.	42
Table 4.3: Coercive field (<i>H_c</i>), saturation magnetization (<i>M_s</i>), remanence (<i>M_r</i>), magneto-crystalline anisotropy (<i>K</i>) and mean square ratio (<i>SQR</i>) of the synthesized compositions.	43
Table 4.4: Real (<i>ε'</i> , <i>μ'</i>) and imaginary (<i>ε''</i> , <i>μ''</i>) parts of permittivity and permeability parameters along with dielectric and magnetic tangent loss (<i>tandε</i> , <i>tandμ</i>) of the synthesized compositions at 1 GHz.	47
Table 4.5: Impedance Matching and Reflection Loss.....	54

LIST OF FIGURES

Figure 1.1: Positioning of microwaves in electromagnetic radiation spectrum	2
Figure 1.2: Pictorial illustration of shielding mechanisms inside a material.....	2
Figure 1.3: The general process of an incident microwave through a microwave absorption material.....	3
Figure 1.4: Mechanism of the electromagnetic wave absorption	4
Figure 1.5: Mechanism of absorption	4
Figure 1.6: Process of Reflection Loss	5
Figure 1.7: Paramagnetic behaviour	7
Figure 1.8: Ferromagnetic behavior.....	8
Figure 1.9: Diamagnetic: Figure 1.2.3.4: Ferrimagnetic behaviour	8
Figure 1.10: Anti-ferromagnetic behavior	9
Figure 1.11: Super paramagnetic behavior	10
Figure 1.12: Cross sectional view of BaFe ₁₂ O ₁₉	15
Figure 3.1: Real time steps of sol-gel auto-combustion technique for the preparation of La-Y substituted BaM nanoparticles.	29
Figure 3.2: Prepared powder samples for XRD analysis.....	30
Figure 3.3: KBr mixed semi-transparent powdered samples for FTIR examination.....	31
Figure 3.4:(a-c): (a). Ultrasonic bath (Cole-Parmer) instrument at SCME, NUST (b). Homogenously dispersed solution in a vial bottle (c). Dry thin films of dispersed solutions for SEM.	32
Figure 3.5: VSM Software.....	33
Figure 4.1: Indexed XRD pattern of the synthesized BaY _x La _x Fe _{12-2x} O ₁₉ , (0.00 ≤ x ≤ 0.050) samples	37
Figure 4.2: Shifting of high intensity peaks towards lower angles with increasing La-Y substitution.....	38
Figure 4.3:(a-d): SEM images of the prepared compositions BaY _x La _x Fe _{12-2x} O ₁₉ ; (0.00 ≤ x ≤ 0.050) nanoparticles; (a). Pure BaFe ₁₂ O ₁₉ (b). BaLa _(0.020) Y _(0.020) Fe _(11.96) O ₁₉ (c).BaLa _(0.035) Y _(0.035) Fe _(11.93) O ₁₉ and (d). BaLa _(0.050) Y _(0.050) Fe _(11.90) O ₁₉	39
Figure 4.4: FTIR spectra (400 – 650 cm ⁻¹) validate the development of octahedral and tetrahedral sites of the synthesized BaLa _x Y _x Fe _{12-2x} O ₁₉ (0.00 ≤ x ≤ 0.050) samples.	41
Figure 4.5: Magnetic hysteresis loops of the synthesized BaLa _x Y _x Fe _{12-2x} O ₁₉ (0.00 ≤ x ≤ 0.050) compositions as function of applied field.....	43
Figure 4.6:(a-d): Frequency dependent of (a). ε' and (b). ε'' (c). μ' and (d). μ'' of the synthesized BaLa _x Y _x Fe _{12-2x} O ₁₉ (0.00 ≤ x ≤ 0.050) samples in the frequency range of 1-18 GHz	48
Figure 4.7: Dielectric loss tangent (tanδ _ε) of La-Y substituted Barium hexaferrite nanoparticles.	51
Figure 4.8: Magnetic loss tangent (tanδ _μ) of La-Y substituted Barium hexaferrite nanoparticles.	52

Figure 4.9:Frequency dependent of reflection loss (RL) of $\text{BaLa}_x\text{Y}_x\text{Fe}_{12-2x}\text{O}_{19}$ ($0.00 \leq x \leq 0.050$) with coating thickness of 2.45 mm in Ku band. 53

LIST OF SYMBOLS, ABBREVIATIONS AND ACRONYMS

BaM	Barium Hexaferrite
MAM	Microwave Absorbing Material
RAM	Radar Absorbing Material
RADAR	Radio Detection and Ranging
RCS	Radar Cross Section
EMI	Electromagnetic Interference
MRI	Magnetic Resonance Imaging
PLD`	Pulsed Laser Deposition
PVDF	Polyvinylidene fluoride
XRD	X-ray Diffraction
FTIR	Fourier Transform Infrared Spectroscopy
SEM	Scanning Electron Microscopy
FESEM	Field Emission Scanning Electron Microscopy
VSM	Vibrating Sample Magnetometer

VNA	Vector Network Analyzer
BSE	Backscattered electrons
SE	Secondary electrons
EM	Electromagnetic

ABSTRACT

Sol-gel auto-combustion was used to successfully produce M-type barium hexagonal ferrite nanoparticles with La and Y co-substitution ($\text{BaY}_x\text{La}_x\text{Fe}_{12-2x}\text{O}_{19}$; $0.00 \leq x \leq 0.050$). The production of a unique hexaferrite phase, with an average crystallite size spanning from 39 to 44 nm was confirmed by X-ray diffraction investigation. The fourier transformed infrared spectroscopy identified three distinct modes (between 400 - 650 cm^{-1}) which are consistent with the typical metal-oxygen bond vibrations at octahedral and tetrahedral sites. Morphological study has revealed that nanoparticles are uniformly scattered and have a spherical shape. Utilizing a vibrating sample magnetometer (VSM) to examine the magnetic characteristics, it was found that when La-Y substitution is increased, substitution is done on Octahedral side and not on Tetrahedral side as La and Y have large ionic radius. Net magnetic moment is decreased when La-Y substitution is increased. Measured using a vector network analyzer, the dielectric and magnetic properties showed an increase in dielectric and magnetic losses with increasing La-Y concentration, indicating improved energy dissipation capabilities. It was observed that the magnetic tangent losses in these nanoparticles were greater than the dielectric tangent losses, suggesting that magnetic losses predominate. With reflection loss values below -10 dB in the Ku band (12–18 GHz), which translates to approximately 90% absorption of incident microwaves, the samples showed strong microwave absorption. With $x = 0.020$, the maximum reflection loss of -23.75 dB was measured with a bandwidth of 5.62 GHz, demonstrating the materials' potential for use in microwave absorption applications.

Keywords: Barium Hexaferrite; Microwave Absorbing Material; Electromagnetic Interference; Magnetic Resonance Imaging

CHAPTER 1: INTRODUCTION

The study and manipulation of materials at the nanoscale are being focused by nanotechnology. Materials frequently display distinctive qualities at this small scale which are used for ingenious applications. The nanomaterials' size, shape, and structure effects its characteristics. Scientists are always experimenting and finding different ways to manipulate these variables in an effort to optimize properties of nanomaterials for particular applications. Higher homogeneity, lower sintering temperatures and benefits of smaller particle sizes frequently leads to enhanced performance materials at nano scale.

On the electromagnetic spectrum, microwaves are the type of waves that fall between radio waves and infrared waves at particular frequency. Their wavelengths range between 1 millimeter to 30 centimeters and their frequencies falls between 30 MHz to 300 GHz. This specific frequency band's signals are regarded as alternating current (AC) signals. Microwaves are widely employed in many different important applications such as communication, radar, stealth and heating technologies. They have a great deal of adaptability in both every day and scientific applications because of their ability to interact and permeate with many materials.

1.1 Background

Modern societies profoundly rely on electromagnetic technologies which is evident from the ubiquitous use of microwaves across various sectors of life. These applications demand appropriate materials for effectively managing, processing microwaves and ensuring that they are safe and do not cause mutual interference. This condition has spurred interest in the study of microwaves interacting with materials which leads towards advancements in both industrial and consumer products [1].

1.2 Microwaves

Microwaves are the segment of electromagnetic spectrum with frequencies ranging from 300 MHz to 300 GHz which are capable of penetrating different media and making them extremely versatile. They are crucial in radar systems for identifying object

characteristics via wave reflection and analysis. In telecommunications, microwaves facilitate the transmission of substantial data over long distances. Household microwave ovens utilize these waves to heat food by exciting water molecules, generating heat through friction [2].

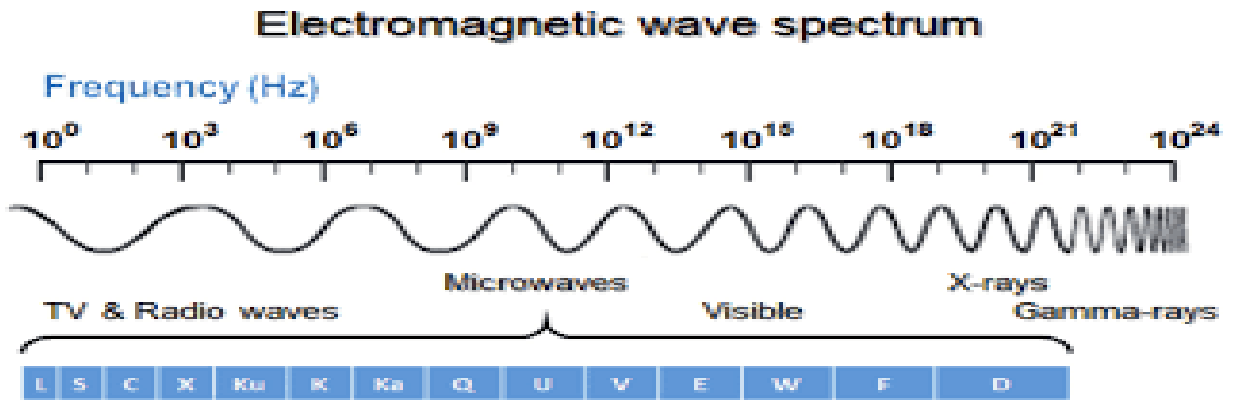


Figure 1.1: Positioning of microwaves in electromagnetic radiation spectrum

1.2.1 Microwave Absorption

Microwave absorption is essential in military and aeronautical contexts to camouflage equipment from radar detection. This involves materials that either absorb and convert harmful microwave energy into heat or trap it, preventing reflection. This functionality enhances stealth capabilities [3].

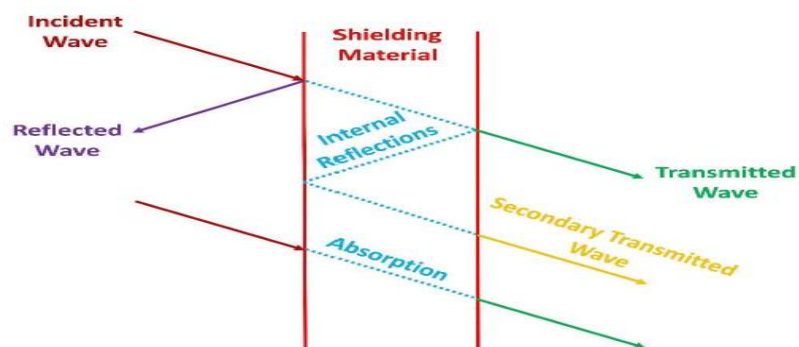


Figure 1.2: Pictorial illustration of shielding mechanisms inside a material.

1.2.2 Microwave Absorbing Materials

A diverse array of materials is used to dissipate or let through maximum microwave energy, typically composed of metal particles, carbon, and polymers. These materials are engineered to selectively absorb certain frequencies while remaining robust under various conditions.

The development of these materials focuses on precise control over composition and structural characteristics to achieve desired electromagnetic properties [4].

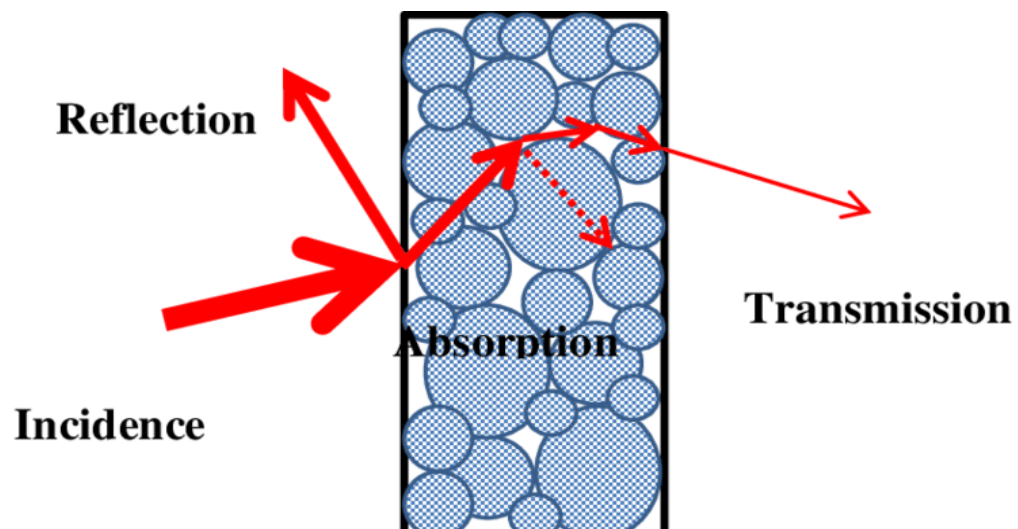


Figure 1.3:The general process of an incident microwave through a microwave absorption material.

1.2.3 Properties Affecting Microwave Absorption

Several material properties are critical in influencing microwave absorption, including:

1.2.4 Magnetic Properties

Materials with strong magnetic properties enhance microwave absorption through mechanisms like magnetic loss. For example, certain ferrites absorb microwave energy and convert it into heat, reducing the wave's amplitude [5].

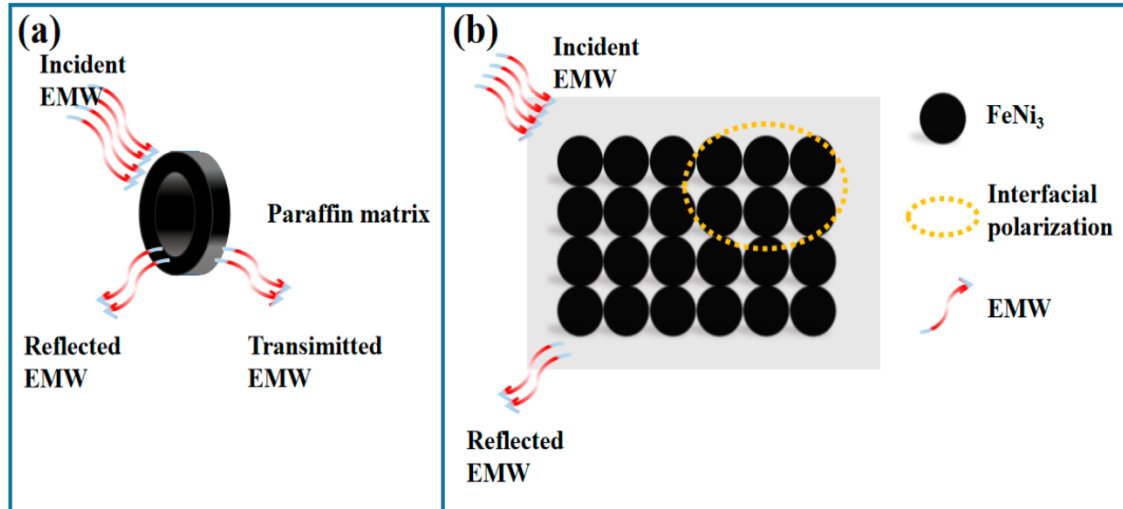


Figure 1.4: Mechanism of the electromagnetic wave absorption

1.2.5 Complex Permittivity & Permeability

High values of permittivity and permeability enable a material to store and dissipate electromagnetic energy more effectively, which is crucial for interacting with both the electric and magnetic components of microwaves [6].

1.2.6 Eddy Current Loss

Materials with high electrical conductivity induce eddy currents when exposed to microwaves, which generate heat through resistive loss and enhance absorption efficiency [7].

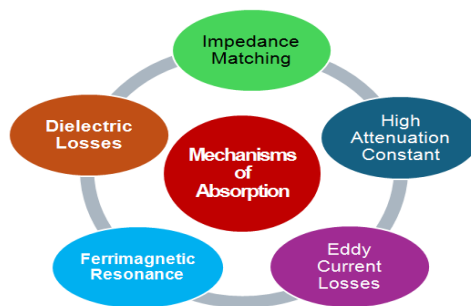


Figure 1.5: Mechanism of absorption

1.2.7 Reflection Loss

When a wave, such as light, sound, or an electromagnetic signal, crosses a barrier between two distinct mediums and some of it is reflected back, it is referred to as reflection loss. This is the decrease in signal power that results.

This phenomenon can cause inefficiencies in systems like optical fibers, transmission lines, or acoustic spaces. It is frequent in the fields of optics, acoustics, and telecommunications. Anti-reflective coatings and impedance matching are two common methods used to reduce reflection loss, which is contingent upon the qualities of the medium involved, including their refractive indices and acoustic impedances.

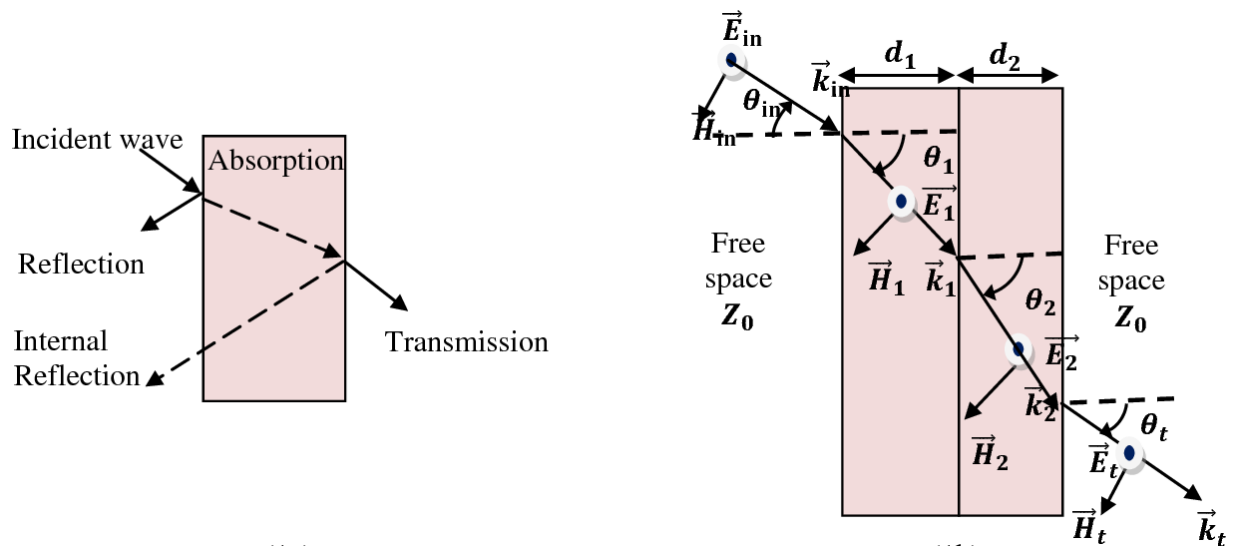


Figure 1.6:Process of Reflection Loss

Minimizing reflection loss is essential in applications where absorption is preferred over reflection. Materials are designed with specific impedance profiles to optimize this balance [8].

1.2.8 Impedance Matching

Effective impedance matching involves adjusting a material's electrical properties to match those of its environment, reducing reflections and enhancing overall efficiency [9].

1.2.9 Attenuation Constant

The attenuation constant shows, how rapidly a material can decrease the intensity of microwave signal as it passes through, and it is crucial for high-frequency applications where rapid energy dissipation is needed [10].

1.3 Introduction to Magnetism

Magnetism in materials is fundamental for a wide range of applications from electronics to magnetic resonance imaging (MRI). Each magnetic behavior influences how materials are used in technologies, particularly in controlling and detecting electromagnetic fields [11].

1.3.1 Magnetism and its Types

The word "magnetic" comes from "Magnesia", an island in the Aegean Sea where lodestone, a naturally magnetic stone, was found near the knowledge of magnetism is ancient, and major advances in its understanding occurred in the 20th century. Chinese used magnets for navigation which was further used in making compass. later in 16th century a physicist named William Gilbert invented artificial magnet and showed that a compass needle always points towards north and south due to magnetism of earth.

In year 1750, scientist named John Michell proposed that magnetic poles follow inverse square law and this theory was also confirmed by Charles Coulomb. The first electromagnet was created in 1825 when scientists discovered that electric current created a magnetic field. Researchers such as Faraday, Becquerel, and Bergmann further explored the effects of magnetism on liquids and gases, identifying materials with significant magnetic properties.

Magnetism is rooted in the concepts of dipoles and magnetic fields where magnetic poles always exist in pairs (north and south). A material's response to a magnetic field defines its magnetism which disappears above a definite temperature called the Curie temperature which is named after scientist named Pierre Curie.

1.3.2 Paramagnetic

It happens as a result of electrons' orbital and spin movements working together in a magnetic field. Even in the absence of an external magnetic field, a permanent dipole moment occurs from the partial cancellation of the spin and orbital magnetic moments of electrons. This characteristic is known as paramagnetic behavior. Materials like certain ceramics and metals are paramagnetic; they align with magnetic fields but do not retain magnetization, important for applications like MRI contrast agents [12].

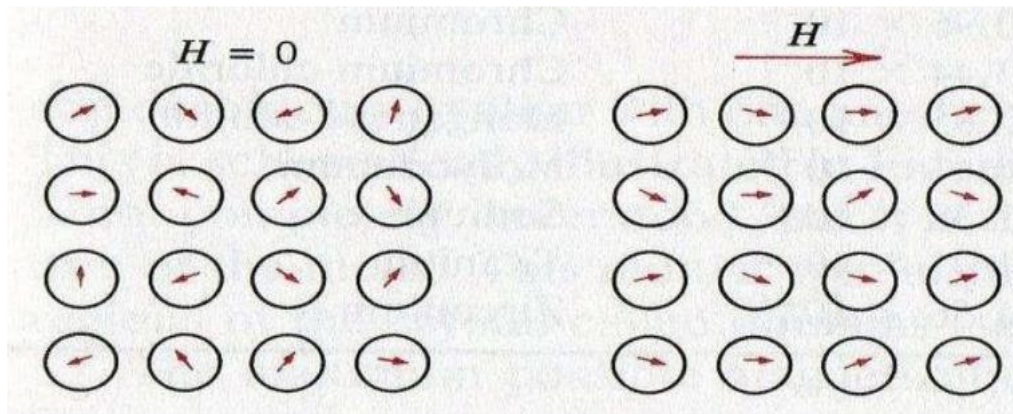


Figure 1.7:Paramagnetic behaviour

1.3.3 Diamagnetic:

Diamagnetic materials, including bismuth and water, exhibit weak repulsion of magnetic fields, critical in applications that require stability against external magnetic influences, like in superconducting magnets [13].

1.3.4 Ferromagnetism

The coupled orbital and spin movements of electrons in magnetic fields give rise to ferromagnetic behavior. Unpaired electrons produce a net magnetic moment because the spin and orbital motions are not completely cancelled. Strong magnetization is produced when an external magnetic field is applied as all dipole moments align with the field. This alignment is maintained until the material reaches the Curie temperature, at which point its magnetic properties vanish, even after the field is removed. Cobalt, iron,

and nickel are examples of ferromagnetic materials that show an extremely high and positive susceptibility to external magnetic fields. Iron and nickel, for instance, not only attract but also retain magnetic properties, foundational for permanent magnets in motors and generators [14].

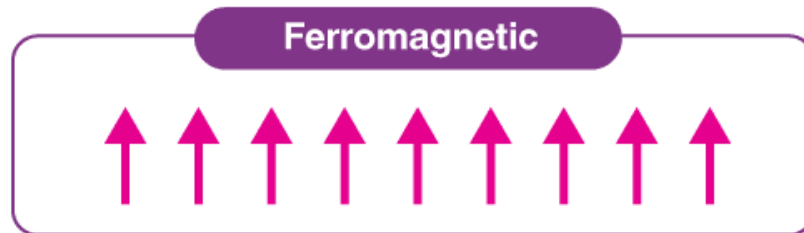


Figure 1.8: Ferromagnetic behavior

1.3.5 Ferrimagnetism

The combined orbital and spin motion of electrons in a magnetic field gives rise to ferrimagnetism. Unlike ferromagnetic materials, ferrimagnets have dipoles that align with the external field and those that oppose it, but the dipoles that oppose are unequal, so the net magnetic moment is smaller than in ferromagnetic materials. For instance, in ferrous ferrite (FeO_4), Fe^{3+} ions at the tetrahedral (B) and octahedral (A) sites have opposite magnetizations, canceling each other out; however, Fe^{2+} ions at the octahedral site add to the net magnetization because their magnetization is not cancelled. Ferromagnetic materials like magnetite have unequal opposing magnetic moments, making them valuable in magnetic recording and data storage [15].

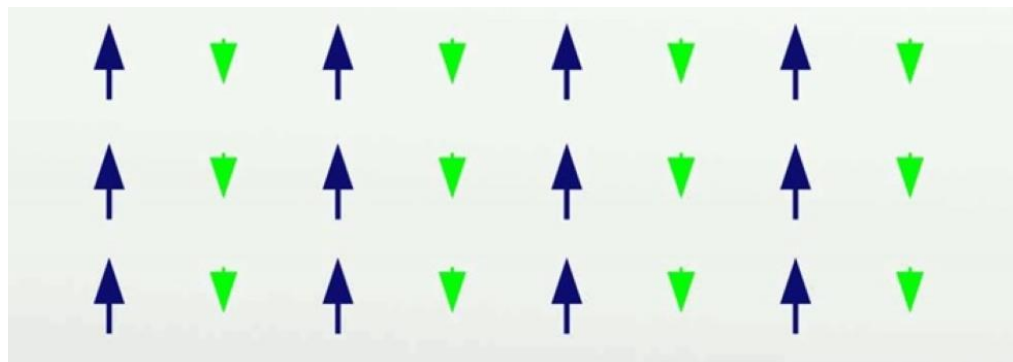


Figure 1.9: Diamagnetic: Figure 1.2.3.4: Ferrimagnetic behaviour

1.3.6 Anti ferromagnetism

Anti ferromagnetic materials have opposite-aligned magnetic moments that cancel out, ideal for minimizing magnetic interference in technologies like MRAM [16]. In the nonexistence of an external magnetic field, anti-ferromagnetic behavior results from the anti-parallel alignment of electron spins in nearby atoms which avert net magnetization. In 1938, this was first noticed in Minnesota. Two lattices magnetized in opposing directions cancel each other's magnetic moments in anti-ferromagnetic materials. A little net magnetization develops in response to an external magnetic field; this magnetization increases with temperature up to the Néel temperature, after which the behavior becomes less pronounced. This is normal behavior when the temperature is low. Anti ferromagnetic materials comprise of elements such as MnO, NiO, Cr, FeO, and CoO.

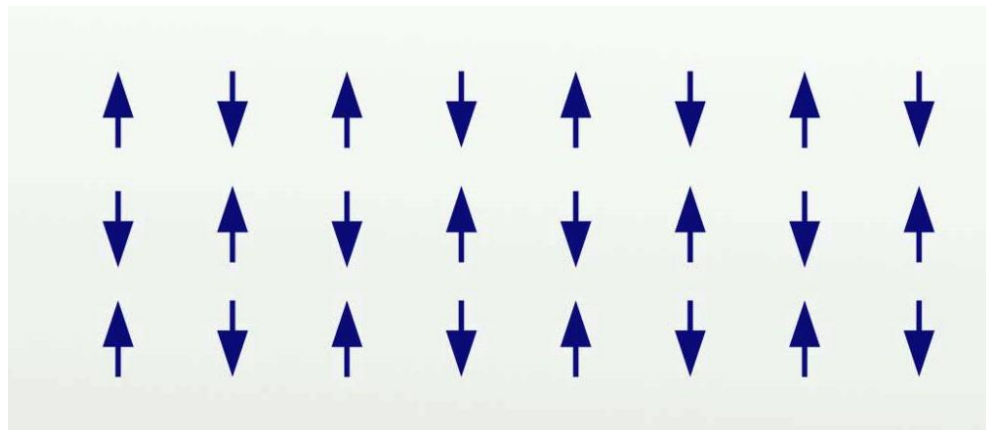


Figure 1.10:Anti-ferromagnetic behavior

1.3.7 Super paramagnetic

The Curie temperature is the point at which a material exhibits paramagnetic behavior below it, or the point at which ferrimagnetic behavior changes to paramagnetic behavior. Neighboring atoms in these materials tend to align, which makes the converted paramagnetic state's magnetic susceptibility significantly greater than that of normal paramagnets. Super paramagnetic materials show magnetic properties only above certain particle sizes and are crucial in medical applications like targeted drug delivery and MRI contrast agents [17].

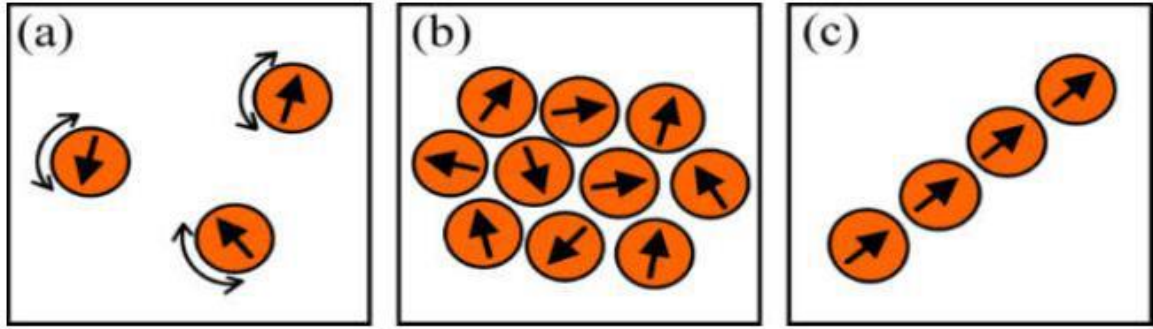


Figure 1.11:Super paramagnetic behavior

1.4 History of Ferrites

Ferrites are ceramic materials made of iron oxides mixed with other metallic elements such as zinc, nickel, and manganese. Ferrites have a long history that dates back to the usage of magnetite (Fe_3O_4) in the first compasses. Ferrites are a family of magnetic materials that are largely made of iron oxide (Fe_3O_4) mixed with additional metals like nickel, zinc, or manganese. Work on ferrites started in 1930s which was the beginning of contemporary ferrite knowledge and synthesis which was mostly done by Japanese scientist named Kato Takei. This led towards the invention of ferrites which are important for electronic devices such as manganese-zinc (MnZn) and nickel-zinc (NiZn). Due to high-frequency capabilities, ferrites became essential to radar technology during World War II which led to further developments. Ferrites are necessary in many fields of life such as electronics, energy storage and telecommunications applications and research work is constantly being done to improve their qualities for new uses in future. Ferrites are used in a variety of applications like transformer cores, electromagnetic interference shielding etc. and play a significant role in the advancement of electronics and magnetic technologies [18].

1.4.1 Ferrites

Ferrites contain ferrimagnetic oxides, so they are considered to be the most significant ferrimagnetic materials. Ferrites are referred to as insulating materials because of their oxides. Iron oxide is ferrite's main constituent. These materials have a magnetic

quality and are utilized in a variety of settings, including transformer cores and permanent magnets. Because ferrites have a high electrical resistance, eddy current production is restricted in them. They are frequently employed in high frequency applications as a result of this feature. Structure and hysteresis losses are the two characteristics used to categorize ferrites. Based on hysteresis losses, Ferrites are classified as hard and soft ferrites.

1.4.2 Soft Ferrites

Primarily utilized in electrical transformers and inductors, soft ferrites exhibit low coercivity and high electrical resistance, minimizing eddy current losses at high frequencies, making them suitable for high-frequency applications [19].

1.4.3 Hard Ferrites

Also known as ceramic magnets, hard ferrites exhibit higher coercivity and are employed in the creation of permanent magnets. Their robust nature and resistance to demagnetization support their use in electric motors and magnetic therapy products [20].

1.4.4 Structural Classification of Ferrites

According to structure, there are three types of ferrites which are classified as:-

- Spinel Ferrites
- Garnet Ferrites
- Ortho Ferrites
- Hexagonal Ferrites

1.4.5 Spinel Ferrites

Known for their cubic crystal structure and moderate magnetic strength, spinel ferrites are used in inductors, transformers, and as noise filters in electronic circuits [21].

1.4.6 Garnet Ferrites

Garnet ferrites are crucial in optical and high-frequency microwave applications due to their unique properties, serving in the manufacture of isolators, circulators, and phase shifters for radar and satellite communications [22].

1.4.7 Ortho Ferrites

With an orthorhombic crystal structure, orthoferrites are known for their large magnetic anisotropy, suitable for high-temperature magnetic applications like sensors and actuators [23].

1.4.8 Hexagonal Ferrites

Also called hexaferrites, these have a complex magnetic structure that provides high coercivity and anisotropy, ideal for permanent magnets and magnetic recording media, especially in applications requiring stable magnetic performance [24].

1.5 Hexaferrites

Hexagonal ferrite's typical formula is $MFe_{12}O_{19}$, where M might be strontium, barium, lead, or any combination of these. Three tetrahedral, octahedral, and trigonal positions in its structure are occupied by metal ions. Owing to their strong coercivity, they are frequently found in refrigerator magnets, microwave applications, loudspeakers, and magnetic recording systems. The most well-known hexaferrite is barium hexaferrite.

1.5.1 Classification of Hexaferrites

Hexaferrites are classified into six different types based on their chemical composition and crystalline structure.

1. M-type ($AFe_{12}O_{19}$) e-g $BaFe_{12}O_{19}$ (BaM) & $SrFe_{12}O_{19}$ (SrM).
2. W-type ($AM_2Fe_{16}O_{27}$), e-g ($BaMe_2Fe_{16}O_{27}$) & $BaCo_2Fe_{16}O_{27}$.
3. X-type ($A_2Me_2Fe_{28}O_{46}$), e-g $Ba_2Co_2Fe_{28}O_{46}$, or Co_2X .

4. Y-type ($A_2Me_2Fe_{12}O_{22}$) e-g $Ba_2Co_2Fe_{12}O_{22}$, or Co_2Y .
5. Z-type ($A_3Me_2Fe_{24}O_{41}$) e-g $Ba_3Co_2Fe_{24}O_{41}$, or Co_2Z .
6. U-type ($A_4Me_2Fe_{36}O_{60}$) e-g $Ba_4Co_2Fe_{36}O_{60}$, or Co_2U .

In M type hexaferrites ions like Ba, Sr or Pb are represented by ‘A’ divalent metal ions are represented by ‘Me’ like Mg or Zn. Our research work deals with synthesis and characterization of M-type hexaferrites.

1.5.2 M-Type Hexaferrites

The general formula for M type hexa ferrite is $A \cdot 6Fe_2O_3$. Divalent ion is represented by ‘A’. Ba^{2+} , Sr^{2+} or Pb^{2+} are its examples. Lattice constants are $a = 5.89 \text{ \AA}$ and $c = 23.19 \text{ \AA}$ for $BaFe_{12}O_{19}$. Barium hexaferrite has been known to researchers from many years. It has a “melting point of 1390°C which was initially affirmed in year 1936. The compound is isomorphous in nature because of which its structure was not affirmed as a hexagonal magnetoplumbite. It was determined on and portrayed concerning its magnetic nature by Philips in mid 1950s. Ferroxdure was the first name given to this compound. The BaM compound has lower saturation magnetization than the other existing alloy magnets, it has high electrical resistivity. Widely used in permanent magnets and electronic components for their high coercivity and magnetic permeability [25].

1.5.3 R-type Hexaferrites

Known for their high resistivity and chemical stability, used in filters and phase shifters in high-frequency circuits [26].

1.5.4 X-type Hexaferrites

Distinguished by their exceptional dielectric properties and suitable for GHz frequency applications in radar and communication systems [27].

1.5.5 W-type Hexaferrites

Known for their large anisotropy fields, used in recording media and microwave devices [28].

1.5.6 Y-type Hexaferrites

Used in multilayer chip inductors and transformers due to their high permeability and low power loss at high frequencies [29].

1.5.7 Z-type Hexaferrites

They are notable for their high electrical resistivity, magnetic anisotropy, ideal for high-density magnetic recording and data storage applications [30].

1.5.8 Properties of Hexaferrites

Hexaferrites sometimes referred to as hexagonal ferrites, have a complicated crystal structure that varies based on its composition but has characteristics in common with each kind. Iron (Fe) cations, which can occupy tetrahedral, octahedral, or hexahedral positions within the crystal lattice, are the primary source of the magnetic characteristics of hexaferrites.

These materials are vital in many applications, including electronics and telecommunications, because of their noteworthy physical, magnetic, microwave, and dielectric properties.

1.5.9 Physical Properties

The physical characteristics of hexaferrites differ substantially from one another. Because of its superior intrinsic hardness, hexaferrites are usually used in the production of permanent magnets.

Ferrites must develop at temperatures of 900°C or above for use in microelectronics. Table provides a summary of some of the key hexaferrites' physicochemical characteristics.

Table 1.1: Physical properties of the main hexaferrites at ambient temperature

Ferrite	Formula	Molecular mass (g)	ρ (g cm ⁻³)	c (Å)	Magnetisation at room temp
BaM	BaFe ₁₂ O ₁₉	1112	5.28	23.18	uniaxial
SrM	SrFe ₁₂ O ₁₉	1062	5.11	23.03	uniaxial
Co ₂ Y	Ba ₂ Co ₂ Fe ₁₂ O ₂₂	1410	5.40	43.56	in plane
Co ₂ Z	Ba ₃ Co ₂ Fe ₂₄ O ₄₁	2522	5.35	52.30	in plane
Co ₂ W	BaCo ₂ Fe ₁₆ O ₂₇	1577	5.31	32.84	in cone
Co ₂ X	Ba ₂ Co ₂ Fe ₂₈ O ₄₆	2688	5.29	84.11	in cone
Co ₂ U	Ba ₄ Co ₂ Fe ₃₆ O ₆₀	3624	5.31	38.16 ^a	in plane

Hexaferrites are known for their hardness and chemical stability, crucial for durability in harsh environments [3]).

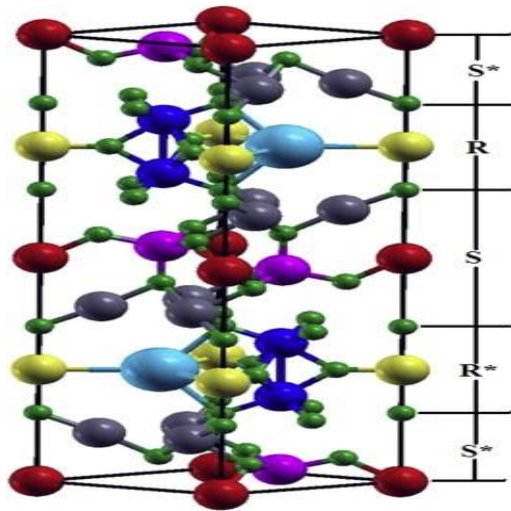


Figure 1.12: Cross sectional view of BaFe₁₂O₁₉

1.5.10 Magnetic Properties

Large metal ions such as Ba or Sr have an effect on the size of the crystal lattice in hexaferrites, which impacts magneto crystalline anisotropy (MCA). In the majority of common hexagonal ferrites, this anisotropy results in a preferential magnetic axis along the c-axis. Because of this, these ferrites have a different X-ray diffraction (XRD) pattern from ferrite samples that are orientated randomly, which is indicative of their special crystallographic alignment and magnetic characteristics.

The magnetic characteristics of hexaferrites can be dramatically changed by substituting other metal ions. For example, anisotropy and magnetization are enhanced when BaM is doped with Al^{3+} , Ga^{3+} , or Cr^{3+} . These dopants change electrical and magnetic interactions inside the crystal lattice which results in enhancing functionality and personalized hexaferrite magnetic properties. Due to high coercivity and remanence, hexaferrites are very effective in permanent magnet applications especially under thermal stress [32].

1.5.11 Dielectric Properties

Permittivity (dielectric constant), AC conductivity, dielectric loss, resistivity, dielectric tangent loss, impedance and electric modulus are important dielectric characteristics of hexaferrites which makes them unique. These characteristics are to be understood for comprehending how the material's electric field is created. Ferrites' principal conduction mechanism is electron hopping between Fe^{2+} and Fe^{2+} ions which greatly affects their electrical behavior. The hopping process affects the material's dielectric characteristics and also improve its overall conductivity which indicates how well it can store and release electrical energy. They are optimized for high frequency uses as their dielectric properties are very helpful in designing antennas and RF components [33].

1.5.12 Synthesis Method of Hexaferrites

Nanoparticles are created via variety of techniques and every technique has its own pros and cons. These methods of synthesis produce nanoparticles with different electrical, magnetic, and structural characteristics as per their structure. Different methods impact properties of the nanoparticles in different ways thus influencing their performance and appropriateness for particular uses based on requirement. The final characteristics of the nanoparticles such as their electrical conductivity, magnetic behavior and structural integrity are determined by the synthesis method used which makes it an important decision. It typically involves a solid-state reaction at high temperatures and sol-gel and hydrothermal methods are best for better particle control [34]. Synthesis Methods for Hexaferrites are as following: -

- Co Precipitation Method.
- Sol Gel Method.
- Micro Emulsion Method.
- Hydro-Thermal Method.
- Sono Chemical Method.
- Solvo Thermal Method.

There are two types of oxide synthesis in the Co-Precipitation Method (creation of oxides directly and another that yields a precursor that needs to be further processed, like drying and calcinations). Metal hydroxides are made from ammonium hydroxide /sodium hydroxide whereas chlorides are removed by washing. The final product is obtained by filtering and calcining of hydroxide. This method works well for creating homogeneous, pure, and fine nanoparticles. When sodium hydroxide is added, the pH level needs to be regulated to prevent the creation of oxide nanoparticles. Furthermore, the molarity of the chemicals utilized, and the pH of the initial precursors have an impact on the nanomaterials' particle size [35-37].

By using the Sol-Gel Method, a gel is produced during solid-state calcination that minimizes atomic diffusion and guarantees a high degree of homogeneity. Although it can be expensive, this method gives you exact control over the finished products. The sol-gel method of synthesis produces materials with outstanding qualities and a wide range of applications in industries including electronics, energy, and optics. [38-39].

By dissolving a surfactant in an organic solvent, the Micro-Emulsion Method creates spheroidal aggregates referred to as "reverse micelles." These micelles are basically "water-in-oil" micro-emulsions, in which surfactant molecules encircle minute water droplets to form water pools. Because of their size, these pools function as miniature reactors, regulating the size of the particles. These micro-emulsions can be effectively used to precipitate ultra-fine ferrite nanoparticles with regulated size and shape [40-41].

The Hydrothermal/Solvothermal Approach is preferred due to its ease of use, affordability, and superior morphology it bestows onto the manufactured nanoferrites. Using an aqueous solution and high vapor pressure, this process forms crystalline structures, including single crystals and films.

This technique allows for the creation of a large variety of morphological crystals, including hollow spheres, nanospheres, nanorod bunches, nanocrystals, nanocubes, and urchin-like crystals, by precisely regulating particle development and solution re-crystallization. The hydrothermal/solvothermal method's adaptability makes it perfect for customizing nanomaterials' size and shape for particular uses[42-43].

Under ultrasonic waves with frequencies higher than 20 kHz, starting materials in the Sono Chemical Technique go through chemical reactions. By using this method, nanostructured materials are created in a variety of inorganic and organic processes. The sonochemical approach has many benefits such as better mixing consistency, increased control over morphology and inhibition of crystal development. It is very successful method for creating high-quality nanomaterials [45-46].

Hydrothermal/Solvothermal approach is being widely used based on affordability, ease of use and capacity to provide nanoferrites with remarkable shape. Using an aqueous solution and high vapor pressure, this technique creates crystalline structures including single crystals and films. A large range of morphological crystals including hollow spheres, nanospheres, nanorods, nanocrystals, nanocubes, nanorod bunches, and urchin-like crystals are also produced through this technology by carefully regulating particle growth and encouraging solution re-crystallization.

The hydrothermal/solvothermal approach is the best option for creating nanomaterials with certain sizes and shapes for a variety of applications due to its flexibility and effectiveness.

1.5.13 Applications of Hexaferrites

M-type hexaferrites like barium hexaferrite are ceramic materials known for their outstanding magnetic properties including high coercivity, strong magnetic anisotropy,

and remarkable thermal stability. These attributes make them highly adaptable for a wide range of applications across various industries. They are most important in modern technological world and serve as key components in permanent magnets for electric motors and generators and enhancing data storage in magnetic recording media. In biomedicine, their biocompatibility and magnetic properties are valuable for targeted drug delivery and MRI contrast agents. Additionally, their ability to absorb microwaves is critical for EMI shielding and stealth technologies.

Overall, M-type hexaferrites play a very important role in driving novelty and efficiency in most of modern applications. Hexaferrites are employed in a wide range of technologies from traditional uses like permanent magnets and transformers to advanced roles in high-frequency microwave devices and also in emerging spintronic devices [46]. Few applications of hexaferrites are as following:

1. Permanent Magnets

- Used in latest electric motors and generators.
- Essential for a variety of electronics and industrial equipment.

2. Magnetic Recording Media

- Enhances storage capacity of hard drives.

3. Biomedical Applications

- Used in targeted drug delivery systems.
- Being used as contrast agents in Magnetic Resonance Imaging (MRI).

4. Electromagnetic Interference (EMI) Shielding

- Absorbs microwaves for protecting electronic devices from interference.
- Used in Stealth technologies for reducing radar detection.

5. Stealth Bases

- Being used in Radar absorption material for dropping radar signature.

6. Antenna Components

- Used in high-frequency applications - satellite and radar communications.

7. Microwave Devices

- Used in circulators and isolators in variety of microwave communication systems.

8. Transformers and Inductors

- Used in power supplies along with radio frequency applications based on its magnetic properties.

9. Magneto-optical Devices:

- Used in applications that include data processing and storage where light and magnetic characteristics interact with each other.

1.6 M-type Barium Hexaferrites

M-type Barium hexaferrites are critical in applications requiring steady magnetic performance across varying conditions which are characterized by a complex hexagonal crystal structure.

They are known for their high magnetic saturation and energy product which are vital in the design of high-performance permanent magnets [47].

1.7 Thesis Scope

This thesis explores the advanced synthesis with detailed characterization and innovative applications of hexaferrites particularly focusing on M-type Barium

hexaferrites with doping of Lanthanum and Yttrium. The study aims to investigate fundamental properties and potential technological applications of these materials and contributing significantly for development of more efficient and higher-performance materials with greater absorption and reflection losses.

1.8 Research Objectives

- Synthesis of high-quality M-type $\text{BaFe}_{12}\text{O}_{19}$ nanoparticles using sol-gel auto combustion technique.
- Enhancing the $\text{BaFe}_{12}\text{O}_{19}$ nanoparticles' microwave absorption efficiency by replacing it with $\text{La}^{+3} - \text{Y}^{+3}$ ions ($\text{BaY}_x\text{La}_x\text{Fe}_{12-2x}\text{O}_{19}$; $0.00 \leq x \leq 0.050$).
- Characterization of substituted $\text{BaFe}_{12}\text{O}_{19}$ nanoparticles.
- Investigation the effect of doping on structural, magnetic and dielectric properties of La-Y substituted barium hexaferrite $\text{BaFe}_{12}\text{O}_{19}$ for enhanced microwave absorption.
 - Analyzing our synthesized compositions' ability to absorb microwaves over a broad frequency range and investigating their permittivity and permeability behavior.

CHAPTER 2: LITERATURE REVIEW

2.1 Barium based Hexaferrites. (BaM)

Numerous studies have been conducted to create hexaferrites utilizing a variety of techniques and their characteristics. On the other hand, a lot of research has been done to determine how different dopants for Ba and Fe affect M-type barium hexaferrites (BaM).

2.2 Literature Study

Thakur, M., et al. (2024) used the sol-gel auto combustion process to manufacture La-Co doped strontium hexagonal ferrites ($\text{SrCo}_{1.5z}\text{La}_{0.5z}\text{Fe}_{12-2z}\text{O}_{19}$). La-Co doping has enhanced the X band's microwave absorption properties. The maximum reflection loss (*RL*) value of -45.61 dB at 8.98 GHz is observed for $z = 0.2$ at coating thickness of 8.1 mm followed by a decline trend of -18.70 for $z = 0.5$. The greatest reflection loss at composition $z = 0.2$ can be attributed to the real and imaginary impedance values, or 0.997 and 0.010, respectively. The growing pattern of La-Co substituted $\text{SrFe}_{12}\text{O}_{19}$'s absorption characteristics makes these synthetic compositions suitable for a range of applications, such as (i) efficient absorbers of microwave radiation, (ii) wireless communications, and (iii) counter surveillance technologies [48].

Khan, M.Z., et al. (2023) used Zr-Y substituted BaSrM nanoparticles produced by sol-gel auto combustion process and calcined at 900 Co for 6 hours to investigate microwave absorption and EMI shielding. While H_c falls for all samples, doping Zr-Y results in increased magnetic and absorption properties, with the maximum values of M_s (56.7 emu/g) and M_r (28.1 emu/g) recorded for $x = 0.35$. These values are then reduced as substitution rises. The values of permittivity ($\epsilon^{\vee, \prime}$) and permeability ($\mu^{\prime}, \mu^{\prime\prime}$) generally increased as the dopant concentration increased, and the maximum reflection loss (*RL*) of -32.27 dB was recorded for $x = 0.35$ at the peak frequency of 6.43 GHz [48].

Garg, A., et al. (2020); studied the yttrium substitution ($\text{Sr}_{1-x}\text{Y}_x\text{Fe}_{12}\text{O}_{19}$; $x = 0.1, 0.2, 0.3$) synthesized via sol-gel auto combustion technique. They partially replaced the

ferric and ferrous ions in $\text{SrFe}_{12}\text{O}_{19}$ by doping it with "Y," which modified the material's microwave absorption properties. Substitution leads to an enhancement of the saturation magnetization and average particle size while decreasing the coercive field because of a decrease in magnetic anisotropy. The maximum reflection loss (RL) of -18.91 at 10.21 GHz was recorded by the researchers for $x = 0.3$ Yttrium concentration and 2.6 mm coating thickness [49].

Godara, S.K, et.al. (2021); examined substitution of Zn-Zr in M-type BaSr hexaferrite ($\text{Ba}_{0.5}\text{Sr}_{0.5}\text{Zn}_x\text{Zr}_x\text{Fe}_{12-2x}\text{O}_{19}$). It was made utilizing a variety of compositions ($x = 0.00 - 1.00$) using the sol-gel auto combustion process. Zn-Zr doping caused a change in the magnetic characteristics, with the highest value "Ms" of 67.37 emu/g reported for $x = 0.4$. In contrast, the substitution of non-magnetic dopants caused a gradual decrease in the coercive field (Hc), which went from 4.936 KOe to 1.029 KOe. This decrease in Hc is explained by the decrease in magneto-crystalline anisotropy (K). Due to local strain created during doping, the crystallite size exhibits a falling trend (100 nm - 43.3 nm) with Zn-Zr doping [50].

In 2010, M.A. Ahmed and colleagues investigated the composition of the $\text{Ba}_{1-y}\text{La}_y\text{Zn}_{0.5}\text{Mg}_{0.5}\text{CoFe}_{16}\text{O}_{27}$. Solid state reaction technique was used to prepare for the values of y ranging from 0 to 0.07. It has been described using SEM and XRD. By raising the value of lattice parameter "a" and decreasing lattice parameter "c," constant volume was verified. We observed both AC and DC conductivity across a temperature range. DC conductivity range from 4.85×10^{-6} to $3.82 \times 10^{-6} \Omega^{-1} \text{cm}^{-1}$. At $y=0.05$, the maximum values of ac conductivity, dielectric, porosity, effective magnetic moment, and curie temperature were noted [51].

A.Haq and M. Anis-ur-Rehman in 2012 studied $\text{Ba}_{1-x}\text{Pb}_x\text{Fe}_{12}\text{O}_{19}$ for the values of $x=0,0.2,0.4,0.6,0.8$ and 1. The co-precipitation approach using NaOH maintained a pH of 13, and the molar ratio of Ba to Fe in the solution remained at 12. The methods used for characterization were SEM and XRD. Pb replacement was shown to increase particle size, and SEM micrographs verified the hexagonal shape. A decrease in coercivity was noted

with an increase in Pb substitution when the VSM hysteresis loop was examined. As Pb substitution occurred, magnetic induction and remanence increased [52].

S. Noushin Ezzati et al in 2015 studied Barium Strontium ferrite synthesis by sol gel method and doped with Ni and Mn with composition of $(\text{Ba}_{0.25}\text{Sr}_{0.75}\text{Fe}_{11}(\text{Ni}_{0.5}\text{Mn}_{0.5})\text{O}_{19})$, and characterized by XRD, FTIR and FESEM FTIR analysis verified the M type hexagonal structure and reported an average particle size of 45 nm. Its absorption in the X-band (8 to 12 GHz) was evaluated using a vector network analyzer [53].

Samira Mandizadeha et al in 2015 studied synthesis of barium hexa ferrite by sol gel mechanism by using ferric nitrate and barium nitrate and characterise it with maleic acid as capping agent. They investigated the magnetic characteristics of barium hexa ferrite using various polymers and VSM. X-ray energy dispersive spectroscopy and scanning electron microscopy were used to examine the effects of the kind of polymer and amount of maleic acid on the characteristics and morphology of barium hexaferrite. It was confirmed that each of these variable parameters had an impact on the sample's morphology and features [54].

Karamveer Chahal et al in 2017 investigates the synthesis of $\text{Ba}_{1-x}\text{Pr}_x\text{Co}_x\text{Fe}_{12-x}\text{O}_{19}$ by sol gel method and using XRD, TGA, FTIR, TEM and VSM which confirms the M-type hexagonal structure in it. They reach average crystallite size in the range of 38 ± 5 nm. By VSM they showed enlarge in coercivity, retentivity and saturation magnetization. FTIR peaks were observed in the range of 430 to 470 cm^{-1} and 550 to 610 cm^{-1} that confirms the formation of tetrahedral and octahedral cluster and also provide an evidence Fe-O bonds stretching vibrations in this range [55].

CHAPTER 3: MATERIALS AND METHODS

3.1 Materials Used

- Barium nitrates $\text{Ba}(\text{NO}_3)_2$
- Pure analytical iron nitrate((III) nonahydrate $\text{Fe}(\text{NO}_3)_3 \cdot 9 \text{H}_2\text{O}$
- Lanthanum Nitrate $\text{La}(\text{NO}_3)_3 \cdot 6\text{H}_2\text{O}$
- Yttrium Nitrate $\text{Y}(\text{NO}_3)_3 \cdot 6\text{H}_2\text{O}$
- Citric acid $(\text{C}_6\text{H}_8\text{O}_7) \cdot 6\text{H}_2\text{O}$
- Deionized water is the first reagent needed to manufacture all of the samples.
- Without undergoing any additional purification, all of the compounds employed in this study's sample preparations had purity levels of at least 99 percent.

3.2 Synthesis of Lanthanum-Yttrium Substituted $\text{BaFe}_{12}\text{O}_{19}$

The M-type La-Y substituted $\text{BaFe}_{12}\text{O}_{19}$ ($\text{BaY}_x\text{La}_x\text{Fe}_{12-2x}\text{O}_{19}$) nanoparticles were prepared using the sol-gel auto-combustion process (synthesis technique as already explained in chapter - 1). The doping concentration for the substitution of $\text{BaFe}_{12}\text{O}_{19}$ is used at the following ratio.

- $x = 0.00$
- $x = 0.020$
- $x = 0.035$
- $x = 0.050$

3.3 Laboratory Equipment & Accessories Used

- Beakers of 2000 ml and Vial bottles of 20 ml
- Magnetic Stirrer of 3 inch and dropper of 5 ml
- Spatula / Crucibles of 150 ml
- Aluminum foil / Butter papers
- Petri dishes
- Digital pH meter / pH strips
- Digital weighing machine
- Hot plate with magnetic stirrers
- Drying Oven
- Mortar and Pestle
- Muffle furnace
- Ultrasonic Bath
- Hydraulic press along with Pellet die set

Equation 3.1 was utilized in the stoichiometric calculations to get the mass for different sample compositions.

$$\text{Mass (g)} = \text{Molarity} \times \text{MolecularWeight} \times 200\text{ml} \div 1000 \quad (3.1)$$

3.4 Materials - $\text{BaY}_x\text{La}_x\text{Fe}_{12-2x}\text{O}_{19}$; ($0.00 \leq x \leq 0.050$)

Without any additional purification, Barium hexaferrite nanoparticles were synthesized using ingredients with a purity of > 99%. Every chemical that was employed was on hand at SCME, NUST Islamabad. Table 3.1 provides chemical details, and Table

3.2 shows the corresponding mass of the chemicals employed in the synthesis process based on calculations of stoichiometric ratios.

Table 3.1: Detail of Chemicals employed in the synthesis process

No.	Name of Chemical	Formula	Molecular Weight
1.	Barium nitrates	Ba(NO ₃) ₂	261.36 g/mol
2.	Iron (III) Nitrate nanohydrate	Fe(NO ₃) ₃ 9 H ₂ O	404.00 g/mol
3.	Citric acid monohydrate	(C ₆ H ₈ O ₇).6H ₂ O	210.14 g/mol
4.	Lanthanum Nitrate	La(NO ₃) ₃ .6H ₂ O	433.01 g/mol
5.	Yttrium Nitrate	Y(NO ₃) ₃ .6H ₂ O	383.01 g/mol
6.	Ammonia Solution	NH ₄ O	-
7.	Deionized Water	H ₂ O	-

Table 3.2: Mass of the chemicals used for syntheses of **BaY_xLa_xFe_{12-2x}O₁₉** as per their stoichiometric ratio.

No.	x	Ba(NO ₃) ₂	Fe(NO ₃) ₃ . 9H ₂ O	La(NO ₃) ₃ .6H 2O	Y(NO ₃) ₃ .6H ₂ O	(C ₆ H ₈ O ₇).6H ₂ O
1.	0.00	0.522 g	9.696 g	-	-	5.463 g
2.	0.020	0.522 g	9.663 g	0.0173	0.0153 g	5.463 g
3.	0.035	0.522 g	9.639 g	0.0303 g	0.1286 g	5.463 g
4.	0.050	0.522 g	9.615 g	0.0433 g	0.0383 g	5.463 g

3.1 Experimental Work

Nanoparticles of La-Y substituted barium hexaferrite ($\text{BaY}_x\text{La}_x\text{Fe}_{12-2x}\text{O}_{19}$; $x = 0.00$, $x = 0.020$, $x = 0.035$, and $x = 0.050$) were produced through the use of the sol-gel auto combustion process.

Precursors of the beginning metal nitrates $\text{Ba}(\text{NO}_3)_2$, $\text{Fe}(\text{NO}_3)_3 \cdot 9\text{H}_2\text{O}$, $\text{La}(\text{NO}_3)_3 \cdot 6\text{H}_2\text{O}$, $\text{Y}(\text{NO}_3)_3 \cdot 6\text{H}_2\text{O}$ were dissolved in DI water with an adequate stoichiometric ratio while the mixture was stirred continuously.

An aqueous solution of citric acid ($\text{C}_6\text{H}_8\text{O}_7$) was combined with a solution of metal nitrate, and the molar ratio of metal to citric was maintained at a constant 1:1 throughout the experiment. The chelating agent that was chosen was citric acid since it was able to inhibit the precipitation of metal nitrates while simultaneously evaporating water content [1, 28].

To keep the pH at seven, NH_4OH solution was added drop by drop, and then continuous stirring was performed at a temperature of one hundred degrees Celsius.

The solution underwent a transformation into a thick brown gel after being heated and stirred continuously for around five to six hours. Furthermore, upon the complete evaporation of water, the gel spontaneously ignited and burned with bright sparks, resulting in the formation of grey flakes.

After that, the flakes were ground with a mortar and pestle, and then they were calcined in a temperature-programmed muffle furnace at 950 degrees Celsius for four hours. This was done in order to convert the flakes into pure hexagonal phase and to remove organic solvents from the samples that were synthesized in order to obtain La-Y substituted Ba-Hexaferrite nanoparticles.

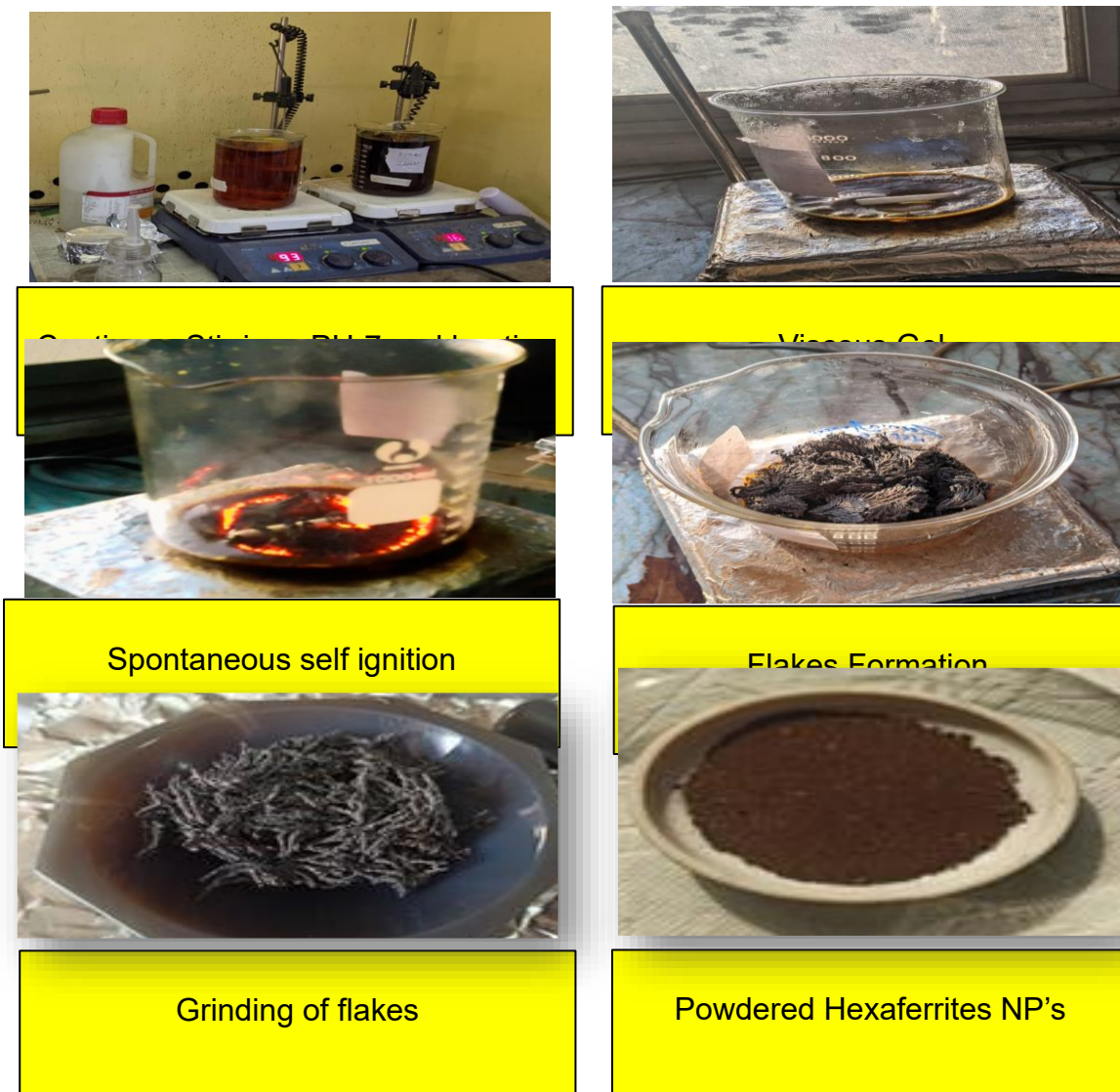


Figure 3.1:Real time steps of sol-gel auto-combustion technique for the preparation of La-Y substituted BaM nanoparticles.

3.5 Sample Preparations for Characterization Techniques

For the purpose of evaluating the SEM, FTIR, VSM, electric, and magnetic properties of the samples, a variety of prepared procedures were utilized. Procedures and their applications for the preparation of various samples are described under the following sections:

3.5.1 Preparation of XRD Samples

An x-ray diffractometer (Bruker D2 Phase Diffractometer) was employed to examine the synthesized compositions' structural properties. Using a mortar and pestle, the samples were thoroughly mashed to produce a homogenous slurry. For every mixture, a sample quantity of 0.5 g was utilized. Prior to XRD analysis, the samples were roasted in a drying oven set to 80 degrees Celsius for 45 minutes in order to eliminate any remaining moisture.

The synthesized compositions were then moved to the XRD apparatus's sample holder (stub) for phase and structural examination. Additionally, since XRD is a non-destructive method, the samples were protected following the analysis. Figure 3.4.1 displays powdered materials ready for XRD examination.



Figure 3.2:Prepared powder samples for XRD analysis.

3.5.2 Preparation of FTIR Samples

The KBr pallet method was chosen for sample preparation due to the fact that alkali salts do not exhibit any absorption in the IR spectrum. The potassium salt was placed in an oven set at 100 degrees centigrade for one hour to eliminate any moisture. Using a small amount of sample and KBr, the mixture was finely ground into a powder. Then, a pallet was carefully prepared using a pallet die set and hydraulic press. Ground mixture of KBr and sample was added into the die and placed into the press. With a pumping movement, the hydraulic pump handle was moved downwards until the scale showed a reading of 3. After patiently waiting for forty-five seconds, the pressure was finally released, and the die was carefully removed. At last, a thin sample pallet with a thickness ranging from 2-3 mm and a diameter of 13 mm was acquired for FTIR.

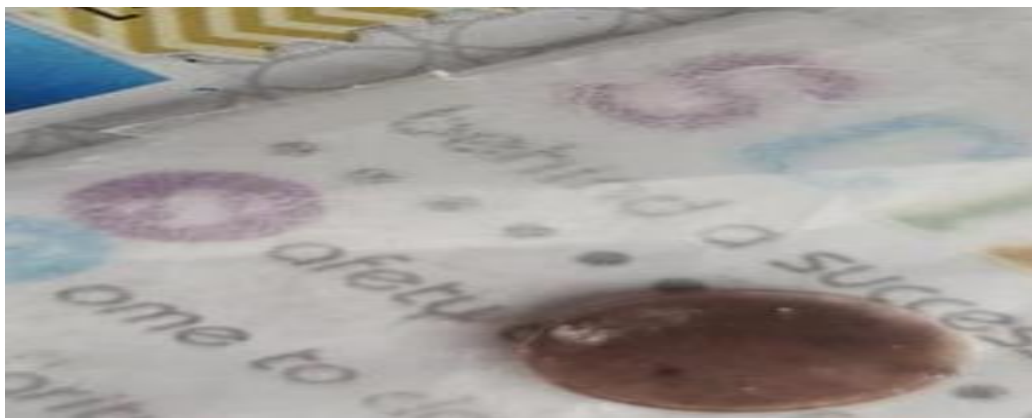


Figure 3.3:KBr mixed semi-transparent powdered samples for FTIR examination.

3.5.3 Preparation of SEM Samples

A homogeneously disseminated solution of the powder sample in deionized water was used for the SEM investigation. Vial vials that had been carefully cleaned with ethanol and dried were filled with a little amount of each mixture and 20 milliliters of deionized water. To create a homogenous and well-dispersed solution, the vial bottles holding the mixes were submerged in an ultrasonic bath (Cole-Parmer) for forty-five minutes. The solution was then dried and drop-cast in order to make it ready for SEM analysis. The substrate surfaces were made of four-piece-cut glass slides.

These slides underwent a thorough ethanol cleaning before being dried for fifteen minutes at 80°C in the oven. Using a 5 ml dropper, the evenly distributed solutions were drop-cast onto the dried slides. Thin layers of powder particles formed on the slides as the water droplets evaporated after heating at 100°C for 30 minutes in a drying oven. Following that, these thin films were secured and readied for morphological examination with a JEOL JSM-6490A model scanning electron microscope (SEM). The illustration of SEM sample preparation is shown in the Figure 3.4.3 (a-c).

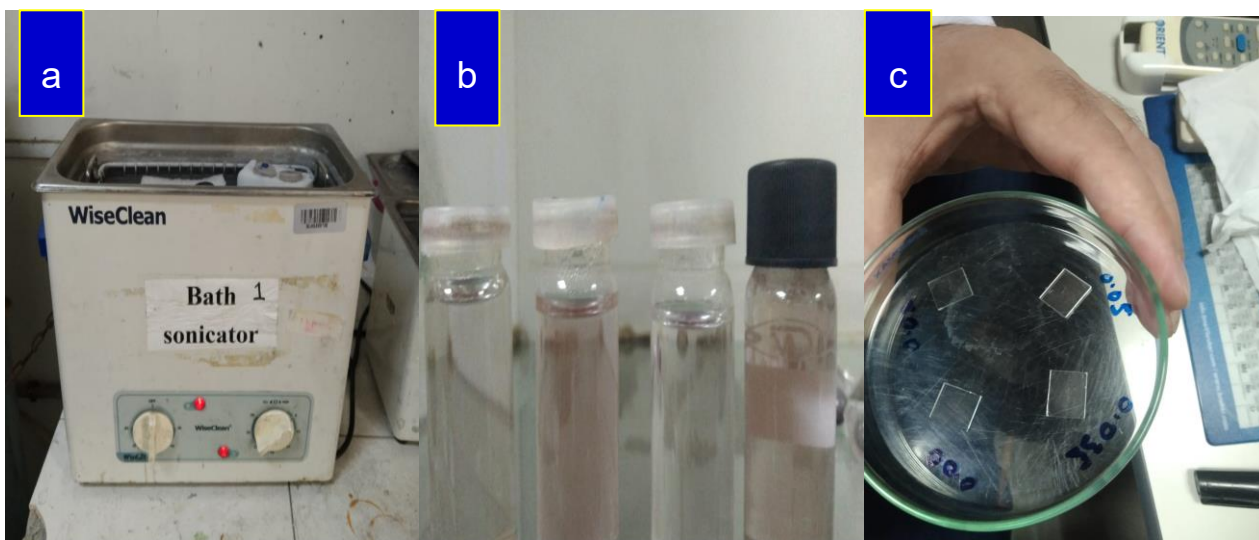


Figure 3.4:(a-c): (a). Ultrasonic bath (Cole-Parmer) instrument at SCME, NUST (b). Homogenously dispersed solution in a vial bottle (c). Dry thin films of dispersed solutions for SEM.

3.5.4 Preparation of VSM Samples

A vibrating sample magnetometer was used to evaluate the synthesized BaM nanoparticles' magnetic characteristics. The powdered nanoparticles were weighed carefully using a digital scale, with 0.05g of each sample being measured.

After measuring the samples, they were put on magnetic tape and firmly secured. After that, a rod that acts as a sample holder was used to put the magnetic tape containing the sample between the pick-up coils, and the vibrating unit was connected to it. This

configuration made it easier to measure the BaM nanoparticles' magnetic properties precisely.

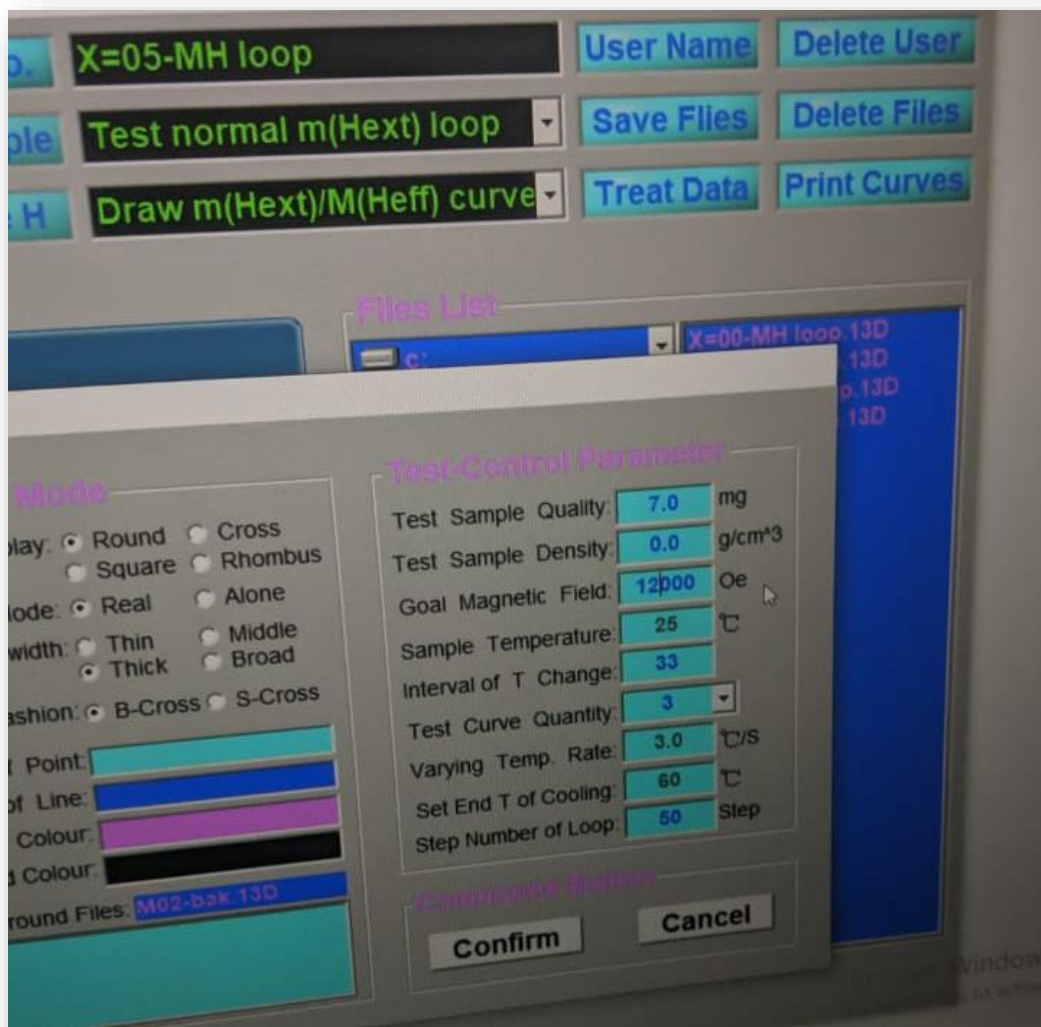


Figure 3.5: VSM Software

3.5.5 Preparation of VNA Samples

The synthesized compounds were well pulverized with a mortar and pestle prior to performing VNA analysis. To evaluate the permeability factor of samples, a toroid-shaped pellets with an inner diameter of 3.02 mm and an exterior diameter of 6.98 mm were created by using toroidal pellet die. It was later subjected to high pressure of 6 tons for three

minutes. In order to find the permittivity parameter of samples, cylindrical-shaped pellets with a diameter of 3.4 mm and a height of 6.7 mm were made using a cylinder mold and high pressure. These pellets were heated at temp of 800°C in a muffle furnace for two hours to remove traces of organic material and contaminants and guaranteeing its structural integrity.

CHAPTER 4: RESULTS AND DISCUSSION

The synthesized $\text{BaY}_x\text{La}_x\text{Fe}_{12-2x}\text{O}_{19}$, ($0.00 \leq x \leq 0.050$) compositions characterization results from XRD, FTIR, SEM, VSM, and VNA analyses have been critically assessed for investigating the effects of La-Y substitution on the structural, dielectric, and magnetic properties of M-type barium hexaferrite nanoparticles. In order to maximize microwave absorption efficiency in the higher frequency range, the study concentrated on how these changes affected complicated permittivity and permeability properties. The results shed light on how La-Y substitution tailors the material's performance for sophisticated microwave absorption applications. The characterization results are being discussed in subsequent paragraphs in a concise and effective manner.

4.1 Structural Analysis (XRD)

The phases and completion of the chemical reaction in a powder sample were confirmed using X-ray diffraction. Important information on X-ray densities and lattice properties was obtained using this method. The structure of the substance was precisely determined by examining the diffraction patterns, which confirmed that the chemical process had finished and that the required phases had been present. The X-ray densities and lattice parameter measurements provided important information about the sample's composition and crystalline structure.

The XRD pattern of all compositions of La and Y substituted Barium hexaferrites having compositions of $x = 0, 0.02, 0.035, 0.050$, were synthesized by sol gel method. Miller indices h, k and l corresponding to the XRD peaks for the compound synthesized are comparable exactly with the standard one of barium hexaferrite [ICDD-00-039-1433] indicating the single hexagonal phase structure of these samples.

The XRD patterns provided represent a structural study of $\text{BaY}_x\text{La}_x\text{Fe}_{12-2x}\text{O}_{19}$, a barium hexaferrite material substituted with La and Y at varying levels of (0.000, 0.020, 0.035, and 0.050). The topmost pattern is a reference (labeled "00-039-1433") corresponding to pure barium hexaferrite ($\text{BaFe}_{12}\text{O}_{19}$) and it serves as a baseline for

comparison against the synthesized materials. For the patterns corresponding to different values of x, the peaks mostly agree with the reference pattern, indicating that the primary hexaferrite structure is preserved despite the substitution. This means that the La and Y ions successfully replace Fe ions without upsetting the overall crystal phase, which is essential for preserving the material's desired properties. Peaks in XRD analysis correspond to specific planes within the crystal structure, and their positions and intensities can reveal information about the crystal phase and any modifications to the structure.

Table 4.1: Crystallite size (D_c), lattice parameters ($a = b, c$), ratio (c/a), d-spacing (d_{hkl}) unit cell volume (V_{cell}), bulk density (ρ_B), x-ray density (ρ_X) and porosity ($P\%$) of the synthesized samples.

S. No	La-Y Contents (x)	D_c (nm)	a (Å)	c (Å)	c/a	d_{hkl} (Å)	V_{cell} (Å ³)
1.	0.00	41.12	6.550	24.979	3.807	2.941	681.36
2.	0.020	41.52	6.559	24.937	3.801	2.944	681.70
3.	0.035	44.14	6.601	24.997	3.751	2.966	683.51
4.	0.050	45.66	6.668	24.875	3.741	2.969	883.79

On increase in value of x, minute changes in intensity and peak positions are evident which suggests that the substitution has altered the lattice parameters. These changes happen when La and Y ions replace Fe within the crystal structure. This causes tiny distortions in the lattice since they are larger than Fe ions. The variations in 2θ positions imply a little expansion or contraction of the unit cell parameters which can change the physical characteristics of the material. In figure 4.2 we clearly observe the shifting of peak toward lower 2θ which indicate due to substitution Ba ion replaces the iron atom expand the lattice. Changes in the degree of crystallinity or preferred orientation of the crystallites, which may be impacted by the level of substitution, may also be responsible for variations in peak intensity. In spite of these modifications, the material remains a single-phase

compound over the range of substitution levels examined because there are no new peaks or appreciable broadening to suggest that secondary phases have developed.

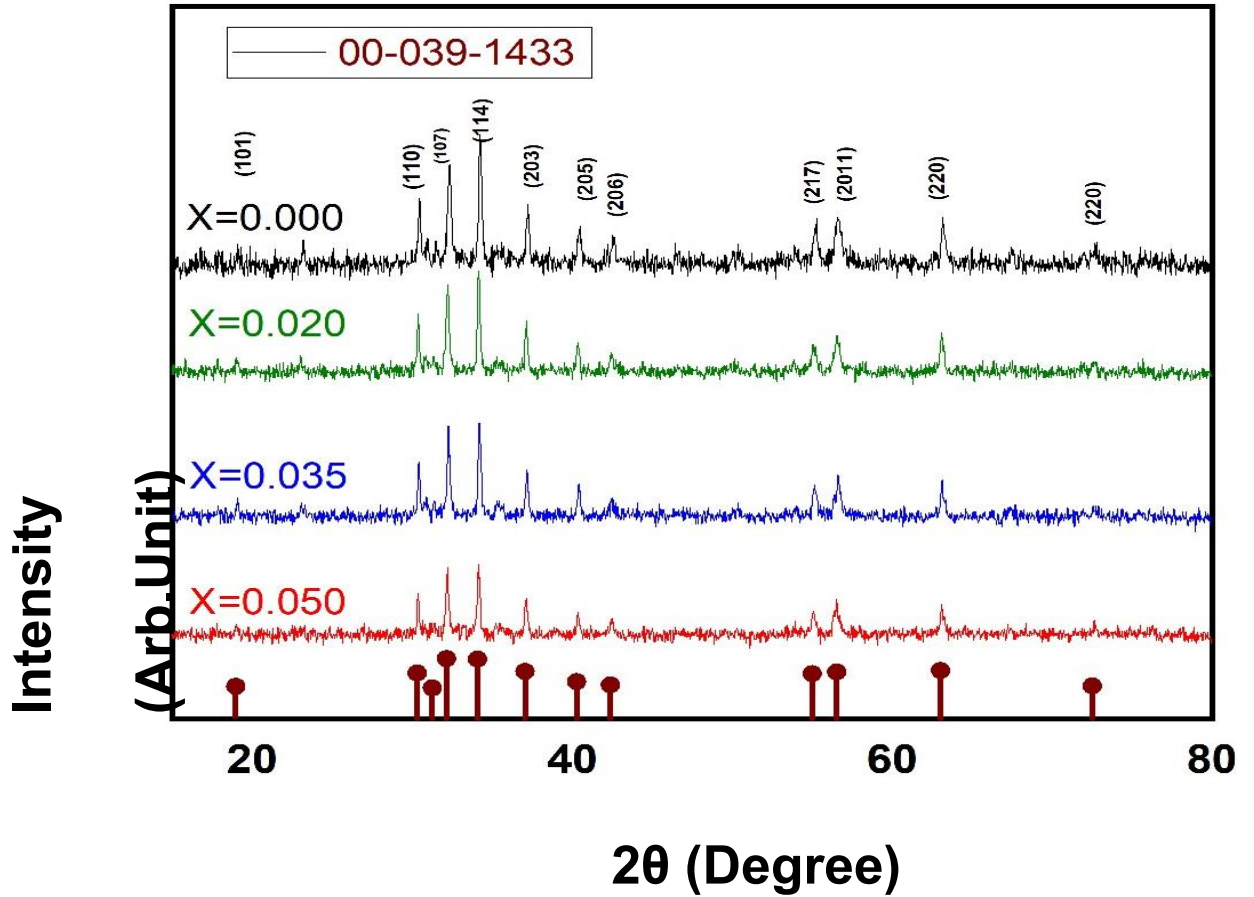


Figure 4.1: Indexed XRD pattern of the synthesized $\text{BaY}_x\text{La}_x\text{Fe}_{12-2x}\text{O}_{19}$, ($0.00 \leq x \leq 0.050$) samples

The preservation of the hexaferrite structure with La and Y substitution has significant implications for the material's magnetic and electronic properties. Permanent magnets, microwaves, and magnetic recording medium are just a few applications for barium hexaferrite where the crystal structure has a direct impact on functionality. La and Y's small lattice distortions may alter the material's saturation magnetization, coercivity, and magnetic anisotropy, which may improve its appropriateness for particular uses. Consequently, it is crucial to comprehend how these replacements effect the crystal

structure in order to modify the material's characteristics to suit particular technical requirements.

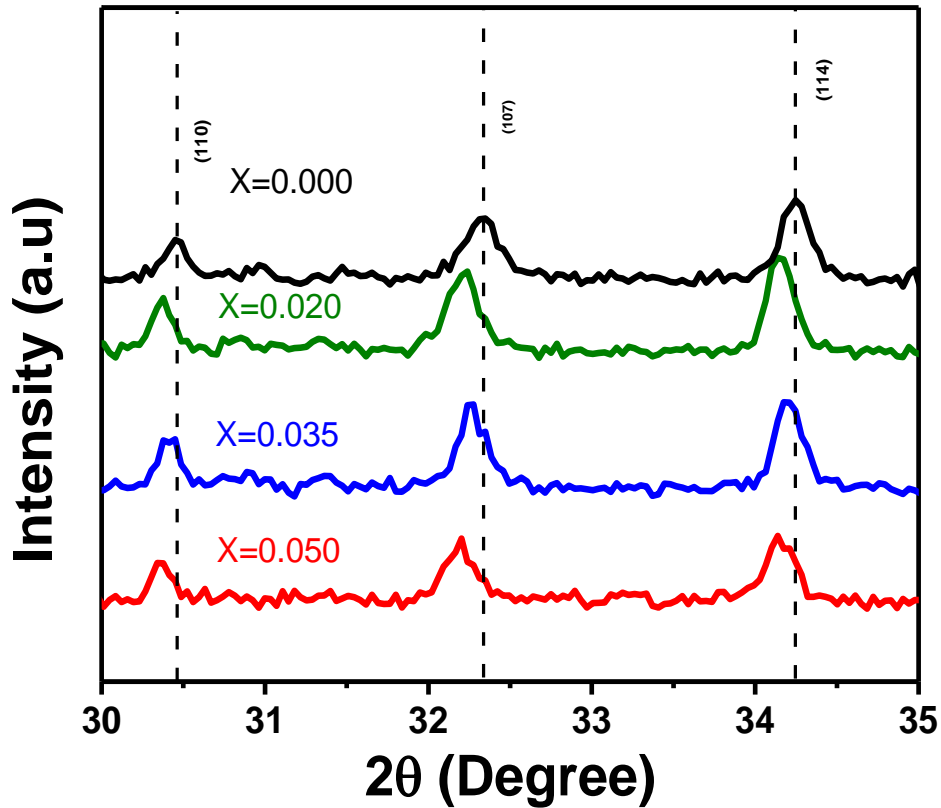


Figure 4.2: Shifting of high intensity peaks towards lower angles with increasing La-Y substitution.

4.2 SEM Analysis (Surface Morphological)

Ferrites are examined microstructurally using the Scanning Electron Microscopy (SEM) technique, which provides important information on phase formation, grain or crystallite size, and sample composition. SEM also aids in determining the material's porosity. The samples were prepared with distilled water and sonicated for two hours each before analysis. This preparation guarantees the best possible imaging and precise microstructure interpretation, enabling a thorough comprehension of the ferrite's overall quality and physical properties.

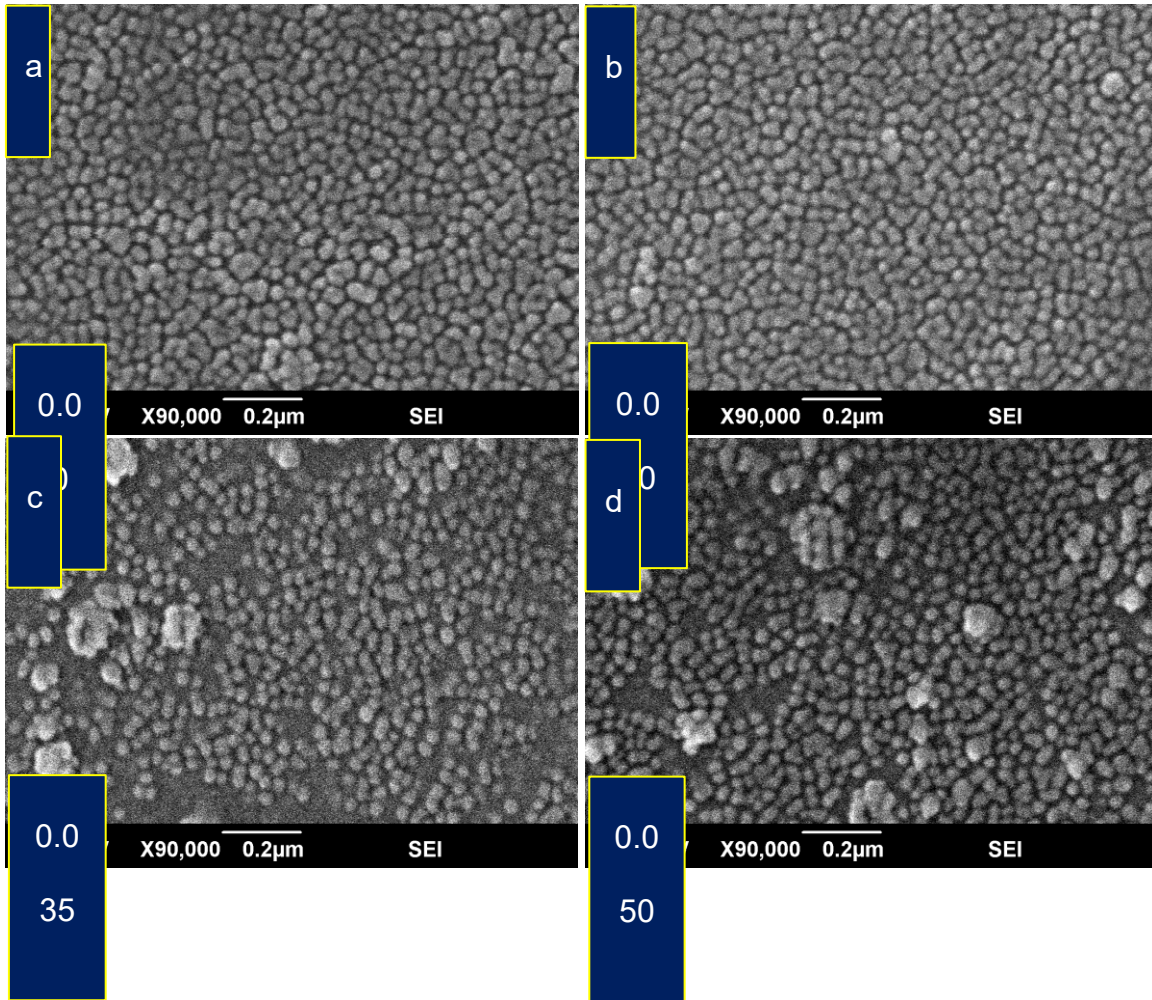


Figure 4.3:(a-d): SEM images of the prepared compositions $\text{BaY}_x\text{La}_x\text{Fe}_{12-2x}\text{O}_{19}$; ($0.00 \leq x \leq 0.050$) nanoparticles; (a). Pure $\text{BaFe}_{12}\text{O}_{19}$ (b). $\text{BaLa}_{(0.020)}\text{Y}_{(0.020)}\text{Fe}_{(11.96)}\text{O}_{19}$ (c). $\text{BaLa}_{(0.035)}\text{Y}_{(0.035)}\text{Fe}_{(11.93)}\text{O}_{19}$ and (d). $\text{BaLa}_{(0.050)}\text{Y}_{(0.050)}\text{Fe}_{(11.90)}\text{O}_{19}$

SEM (JSM-6490A) running at 20 kV with magnification ranging from X8 to X300000 was utilized to investigate the particle size and structural morphology of $\text{BaFe}_{12}\text{O}_{19}$ samples that were replaced with Lanthanum and Yttrium ions. The compositions were pulverized finely in a mortar and pestle after being calcined at 950°C for 4 hours. This allowed for atomic diffusion and correction inside the crystal lattice. The BaM nanoparticles were able to arrange themselves into the lowest interface energy configuration thanks to this procedure. After dispersing the ground components in 20 ml of deionized water in a glass vial, the mixture was sonicated for forty-five minutes. Next,

the suspension was drop-cast onto spotless glass slides in the form of thin films. Using a sputter coater (JFC1500), a tiny layer of gold, only a few nanometers thick, was applied to improve conductivity for SEM imaging and allow for in-depth micro structural study.

4.3 FTIR Analysis

The FTIR spectra obtained for the synthesized compositions ($0.00 \leq x \leq 0.050$), within the IR range of $4000 - 1000 \text{ cm}^{-1}$ as depicted in figure 4.3 while data derived from these spectral lines are presented in Table 4.2. The FTIR spectra of $\text{BaY}_x\text{La}_x\text{Fe}_{12-2x}\text{O}_{19}$, displaying peaks at 440 cm^{-1} , 500 cm^{-1} , and 600 cm^{-1} , can be correlated with microwave absorption properties by examining the material's structural modifications and their impact on electromagnetic properties.

4.3.1 *Vibrational Modes and Permittivity*

The peaks in the FTIR spectra are related to the Fe-O bonds in the hexaferrite structure through vibrational modes. The polarizability of the material is shown by these vibrations. These modes are impacted by the substitution of La and Y, indicating modifications in the dipole moments of the material, which subsequently impact the real (ϵ') and imaginary (ϵ'') components of permittivity. As ϵ' is associated with energy storage and ϵ'' with energy dissipation, these vibrational frequency fluctuations indicate changes in the material's capacity to store and release microwave energy.

4.3.2 *Enhanced Microwave Absorption*

A stronger interaction with the incident infrared radiation is shown by the overall decrease in transmittance with increasing doping concentration (x), which may imply a commensurate increase in microwave absorption. Better impedance matching and greater dielectric losses are probably the results of the structural changes shown in the FTIR peaks, which also boost microwave absorption.

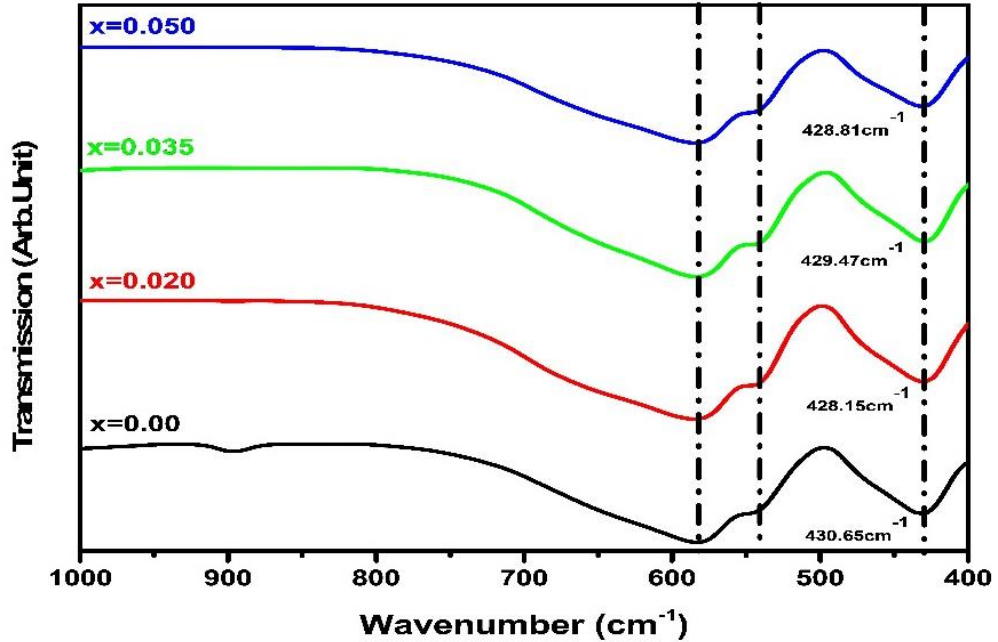


Figure 4.4: FTIR spectra (400 – 650 cm⁻¹) validate the development of octahedral and tetrahedral sites of the synthesized BaLa_xY_xFe_{12-2x}O₁₉ (0.00 ≤ x ≤ 0.050) samples.

FTIR data provides valuable insights of incorporation of La and Y into BaFe₁₂O₁₉ affects the vibrational modes of material which are directly related to its dielectric and magnetic properties. The FTIR spectra exhibit shifts and changes that show these chemical alterations, which are essential for comprehending and enhancing the material's microwave absorption capability. The material is a good option for applications in microwave absorption and electromagnetic interference (EMI) shielding because of its improved impedance matching, enhanced dielectric and magnetic losses, and ability to absorb and dissipate microwave radiation.

Table 4.2: Represents the band positions for an octahedral and two tetrahedral (Fe-O and Me-O) vibrational modes of the synthesized samples.

Composition(x)	Band Position (cm ⁻¹)		
	ν_1 (Tetrahedral)	ν_2 (Octahedral)	ν_3 (Tetrahedral)
x = 0.00	582.23	540.92	430.65
x = 0.020	583.94	541.75	428.15
x = 0.035	582.76	542.10	429.47
x = 0.050	581.75	541.57	428.81

4.4 Magnetic Hysteresis

Using an applied field of 10 kOe, the magnetic characteristics of the produced BaLa_xY_xFe_{12-2x}O₁₉nanoparticles doped with La-Y ions at different compositions ($0.00 \leq x \leq 0.050$) were investigated at ambient temperature. The magnetic hysteresis loops that are supplied show the results, and the table contains a tabulation of the associated parameters.

Table 4.3: Coercive field (H_c), saturation magnetization (M_s), remanence (M_r), magneto-crystalline anisotropy (K_1) and mean square ratio (SQR) of the synthesized compositions.

S. No	Composition x	H_c (Oe)	M_s (emu/g)	M_r (emu/g)	K_1 (erg/cm ³)	SQR (M_r/M_s)
1.	0.00	5111	52.45	31.22	116701.3	0.599
2.	0.020	4837	51.25	30.45	118387.5	0.594
3.	0.035	5002	47.79	29.38	114480.9	0.615
4.	0.050	4990	40.89	24.59	104494.4	0.601

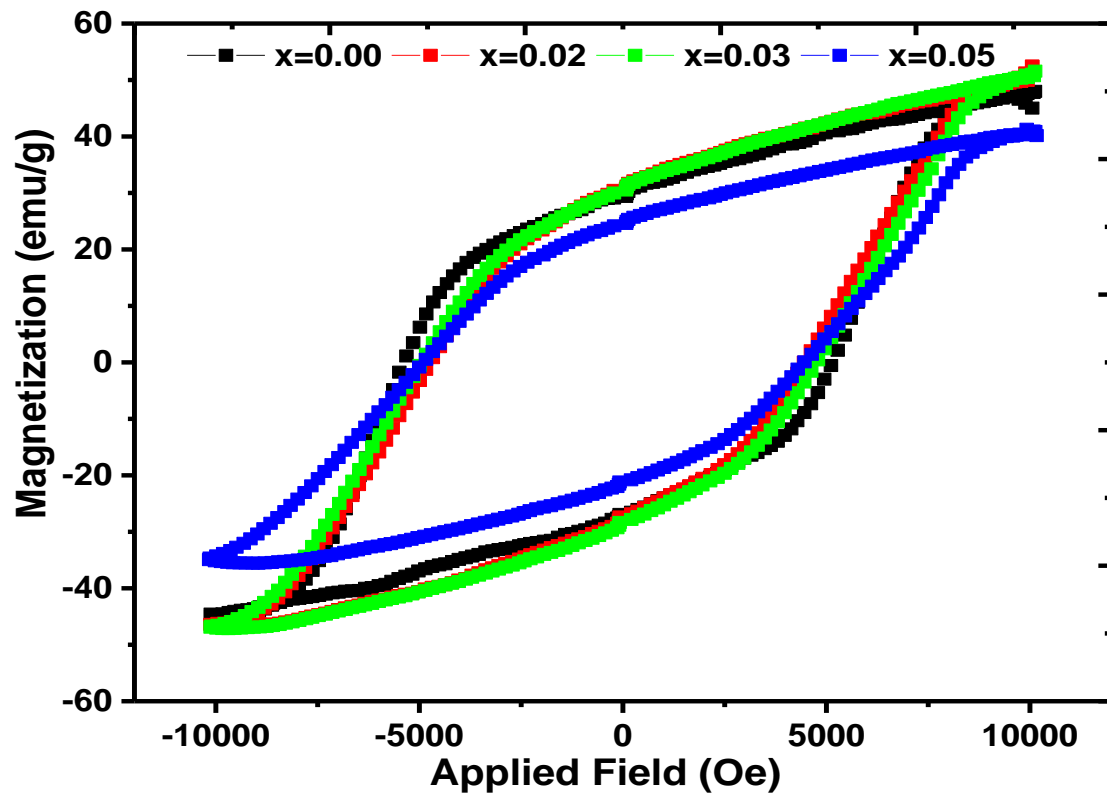


Figure 4.5: Magnetic hysteresis loops of the synthesized $BaLa_xY_xFe_{12-2x}O_{19}$ ($0.00 \leq x \leq 0.050$) compositions as function of applied field.

The magnetic hysteresis loops showed that the compositions performed in a ferromagnetic manner. The enormous size and strong coercive field (H_c) exhibited by these loops suggest hard magnetic behavior. The coercive field values in this instance are greater than 103 Oe, indicating that the material is resistant to demagnetization.

At lower magnetic fields, each hysteresis loop exhibits a noticeable enhancement in magnetization (M), which is stronger as the applied magnetic field increases. The undoped sample ($x = 0.00$) has a significantly higher slope than the doped samples. The saturation magnetization (M_s) was determined using the law of approach (LA) to the saturation method, which involves the linear extrapolation of M versus $1/H$ as H approaches zero.

By changing the balance of magnetic ions inside the crystal lattice, the substitution of La^{+3} ions into the $\text{BaLa}_x\text{Y}_x\text{Fe}_{12-2x}\text{O}_{19}$ ferrite structure have a major impact on its magnetic characteristics. Because there are a lot of Fe^{+3} ions present in the pure form ($x=0.00$), the material exhibits significant magnetic interactions, which raise the net magnetic moment. The total magnetic moment is decreased when fewer magnetic ions are present when La^{+3} replaces some of these Fe^{+3} ions with rising x . The drop in saturation magnetization (M_s) and remanent magnetization (M_r) that is noticed when x grows is a result of this reduction. The decreasing values of M_s indicate a decreased maximum magnetization because there are fewer magnetic ions available to align under an external magnetic field.

Concurrently, an increase in the coercive field (H_c) results from the substitution of La^{+3} ions, suggesting that the material becomes more difficult to demagnetize. The rise in H_c implies that the La^{+3} ions may create lattice distortions or enhance the magneto-crystalline anisotropy of the material. Coercivity is a measure of the resistance to changes in magnetism. These modifications may lead to a stronger pinning of the magnetic domain walls, which would make it harder for them to move and necessitate a higher external magnetic field in order to cause the magnetization to reverse. This pattern is evident in the data in the table, where H_c increases as x increases despite a general decrease in magnetization.

La substitution has an effect on the material's dielectric and permeability characteristics in addition to its magnetic properties. Ferrites' dielectric response and their capacity to polarize in the presence of an external electric field are strongly correlated. The dielectric characteristics frequently go toward lower frequencies as the La content rises. This shift suggests a delayed material reaction to applied field changes, which may be brought about by longer dipole or charge carrier relaxation durations. La^{+3} addition may result in more crystal lattice imperfections or distortions, which would slow down the polarization response. It appears from the material's inferior dielectric response at lower frequencies that it can no longer sustain high-frequency electric fields as well.

Likewise, the La substitution has an impact on the magnetic permeability as well, which gauges the material's capacity to sustain the creation of a magnetic field inside of it. The ease with which magnetic domains align with an external field determines the permeability; the introduction of La^{+3} can impede this alignment. The reason behind the material's decreased sensitivity to high-frequency magnetic fields could be attributed to alterations in the domain wall energy or the total magnetic coupling between ions. A shift in permeability toward a lower frequency suggests that the material's magnetic domains are responding more slowly, maybe as a result of the La substitution's introduction of higher energy barriers for domain wall movement.

La^{+3} ions are substituted into $\text{BaLa}_x\text{Y}_x\text{Fe}_{12-2x}\text{O}_{19}$, which leads to a complicated interplay of changes in permeability, dielectric, and magnetic characteristics. As non-magnetic La^{+3} ions replace magnetic Fe^{+3} ions, the net magnetic moment decreases, resulting in a drop in saturation and remanent magnetization. The material may become more resistant to demagnetization as a result of greater anisotropy or domain wall pinning effects, as indicated by the increase in coercivity. Furthermore, the dielectric and permeability responses' changes towards lower frequencies suggest that the material's reactivity to high-frequency electric and magnetic fields is diminished, maybe as a result of the La substitution's inducing enhanced disorder or relaxation durations. These results highlight the many ways in which magnetic materials' functional properties can be tailored through chemical substitution.

4.5 Microwave Absorption

The microwave absorption efficiency of $\text{BaFe}_{12}\text{O}_{19}$ nanoparticles doped with lanthanum (La) and yttrium (Y) was examined by a thorough analysis that emphasized energy dissipation behavior and reflection loss (RL). The purpose of the study was to investigate how doping affected the material's electromagnetic characteristics, specifically its permeability and permittivity. With the help of an Agilent Network Analyzer, which offered accurate measurements over a broad frequency range, these crucial characteristics were carefully investigated. The material's capacity to store electric energy is shown by its permittivity (ϵ), whilst its permeability (μ) shows that it can facilitate the creation of magnetic fields. The effectiveness with which the doped nanoparticles absorb microwave radiation was shown by calculating the reflection loss (RL), which was computed by examining these characteristics. The results shed light on the potential of La and Y doping to enhance the microwave absorption capabilities of $\text{BaFe}_{12}\text{O}_9$, making it a promising candidate for applications in electromagnetic interference (EMI) shielding and other high-frequency technologies.

4.5.1 Complex Permittivity and Complex Permeability

In order to comprehend the absorption of microwave radiation, the complex permittivity (ϵ) and permeability (μ) are investigated throughout the microwave spectrum, ranging from 1 to 18 GHz, as seen in Figure 4.6(a - d). The resulting data is compiled in Table 4.4. The energy storage and retention from the electric and magnetic components of the incident electromagnetic field are represented by the real parts of permittivity (ϵ') and permeability (μ'), respectively. These characteristics show how much energy the material can hold. On the other hand, the imaginary components (ϵ'') and (μ'') symbolize the dissipation of energy via loss mechanisms, revealing the amount of energy dissipated as heat or other forms. When taken as a whole, these factors offer a thorough picture of the relationship between materials and microwave radiation, including the ratio of energy stored to dissipated.

Table 4.4: Real (ϵ' , μ') and imaginary (ϵ'' , μ'') parts of permittivity and permeability parameters along with dielectric and magnetic tangent loss ($\tan\delta\epsilon$, $\tan\delta\mu$) of the synthesized compositions at 1 GHz.

Sr. No	Sample	ϵ' (1 GHz)	ϵ'' (1 GHz)	$\tan\delta\epsilon$ (1 GHz)	μ' (1 GHz)	μ'' (1 GHz)	$\tan\delta\mu$ (1 GHz)
1.	0.00	2.774	1.663	0.599	3.275	2.785	0.850
2.	0.020	2.470	0.698	0.254	1.081	0.320	0.296
3.	0.035	2.429	0.651	0.254	1.068	0.924	1.078
4.	0.050	2.510	1.290	0.503	1.362	1.401	1.028

Graph in (a) represents the real part of the complex permittivity (ϵ') as a function of frequency for different doping levels of the compound $\text{BaLa}_x\text{Y}_x\text{Fe}_{12-2x}\text{O}_{19}$. The real part of permittivity (ϵ') measures the material's ability to store electric energy when subjected to an external electric field. In this graph in (a), the black line ($x=0.00$) consistently shows the highest ϵ' across the frequency range, suggesting that the undoped material has the best capability for electric energy storage. The slight fluctuations in ϵ' as the frequency increases indicate how the material's electric energy storage capability changes at different frequencies. The red curve ($x=0.020$), on the other hand, shows a noticeable dip in ϵ'' around the 4-6 GHz range, indicating that at this doping level, the material's ability to store electric energy diminishes significantly at these frequencies. The green and blue curves ($x=0.035$ and $x=0.050$) exhibit relatively stable behavior, though they are lower than the undoped material. This suggests that increasing the doping level generally reduces the material's ability to store electric energy, especially at specific frequencies where interactions within the material become more complex.

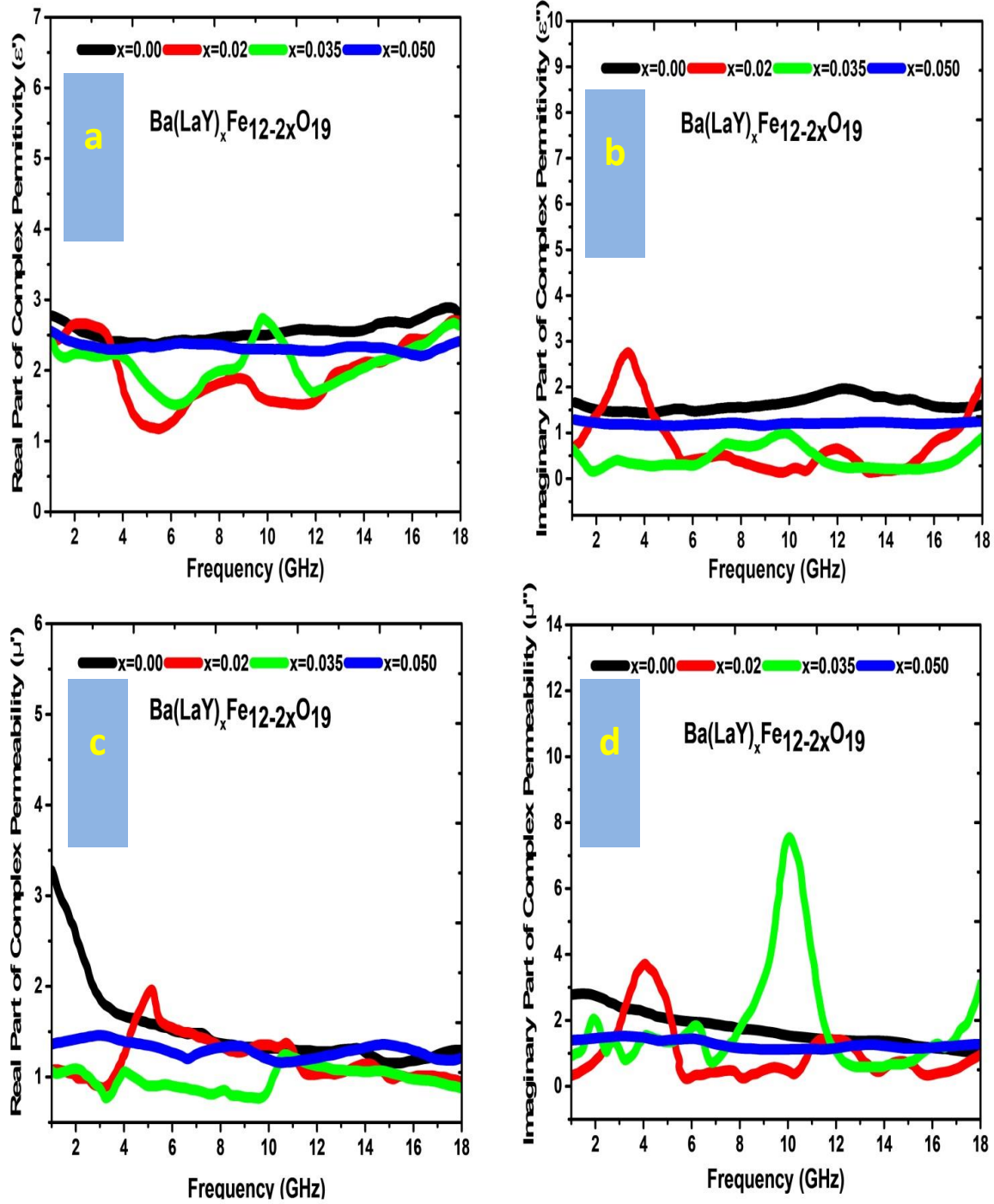


Figure 4.6:(a-d): Frequency dependent of (a). ϵ' and (b). ϵ'' (c). μ' and (d). μ'' of the synthesized $\text{BaLa}_x\text{Y}_x\text{Fe}_{12-2x}\text{O}_{19}$ ($0.00 \leq x \leq 0.050$) samples in the frequency range of 1-18 GHz

Graph in (b) illustrates the imaginary part of the complex permittivity (ϵ''), which is related to the dielectric losses within the material. The imaginary part (ϵ'') indicates how much electric energy is dissipated as heat rather than stored when the material is exposed to an electric field. In this graph, the black line ($x=0.00$) is relatively low and stable across all frequencies, suggesting that the undoped material experiences minimal dielectric losses. This stability is important in applications where efficient energy storage with minimal heat dissipation is crucial. However, the red curve ($x=0.02$) shows a significant peak around the 4-6 GHz range, indicating that at this frequency, the doped material experiences higher energy losses. This could be due to increased interactions or other internal mechanisms in the material at this specific doping level and frequency. The green and blue curves show lower, more stable ϵ'' values, suggesting that while the doping reduces dielectric losses slightly compared to the undoped material, certain doping levels can introduce frequency-dependent energy dissipation peaks, which might limit the material's effectiveness in high-frequency applications.

Graph in (c) shows the real part of the complex permeability (μ'), which indicates the material's ability to support the formation of a magnetic field. The real part of permeability is crucial for understanding how well a material can store magnetic energy. In this graph, the black curve ($x=0.00$) initially shows the highest μ' values at lower frequencies, reflecting a strong ability to conduct magnetic flux. However, as the frequency increases, μ' decreases significantly, demonstrating that the material's magnetic energy storage capability diminishes at higher frequencies. This trend is typical for magnetic materials as their permeability often reduces with increasing frequency due to factors such as eddy currents and domain wall motion. The doped samples, represented by the red, green, and blue curves, exhibit much lower and relatively flat μ' values across the frequency range. This indicates that doping reduces the material's magnetic permeability, which may be beneficial or detrimental depending on the intended application. For example, lower permeability might reduce magnetic losses at high frequencies, but it also means that the material is less effective at supporting magnetic fields.

Graph in (d) shows the imaginary part of the complex permeability (μ''), which is associated with magnetic losses in the material. The imaginary part (μ'') reflects how much magnetic energy is dissipated as heat, rather than being effectively stored in the magnetic field. In the graph, the green curve ($x=0.035$) displays a significant peak around 6 GHz, indicating that at this frequency and doping level, the material experiences increased

magnetic losses. This suggests that the material is less efficient in storing magnetic energy at this specific frequency, which could be problematic for applications requiring high magnetic efficiency at high frequencies. The black curve ($x=0.00$) remains relatively flat and low, highlighting that the undoped material has minimal magnetic losses across the frequency range, making it more suitable for applications where maintaining low energy dissipation is crucial. The red and blue curves (for $x=0.020$ and $x=0.050$) also show some fluctuations but remain lower than the green curve, indicating moderate magnetic losses. These observations suggest that while doping can introduce additional loss mechanisms at certain frequencies, careful selection of the doping level could optimize the material's performance in specific frequency ranges.

4.5.2 Dielectric Loss Tangent

Figure 4.3 illustrates the dielectric loss tangent ($\tan\delta\epsilon$), which is the ratio of the imaginary part to the real part of permittivity ($\tan\delta\epsilon=\epsilon''/\epsilon'$). This ratio provides a measure of how efficiently the material stores electric energy versus how much is lost as heat. In the graph, the red curve ($x=0.020$) exhibits a prominent peak around the 4-6 GHz range, indicating that the material at this doping level experiences significant energy losses in this frequency range.

This peak suggests that the material is less efficient at storing electric energy and instead dissipates a considerable amount as heat, which could be detrimental for high-frequency applications where energy efficiency is critical. The black curve ($x=0.00$) shows the lowest loss tangent across the frequency range, indicating that the undoped material is more efficient in storing electric energy with minimal losses.

The green and blue curves, representing higher doping levels, show relatively stable but slightly higher loss tangents compared to the undoped material, particularly at higher frequencies. This suggests that while doping generally increases dielectric losses, the increase is not uniform across all frequencies, and specific doping levels may introduce frequency-dependent inefficiencies.

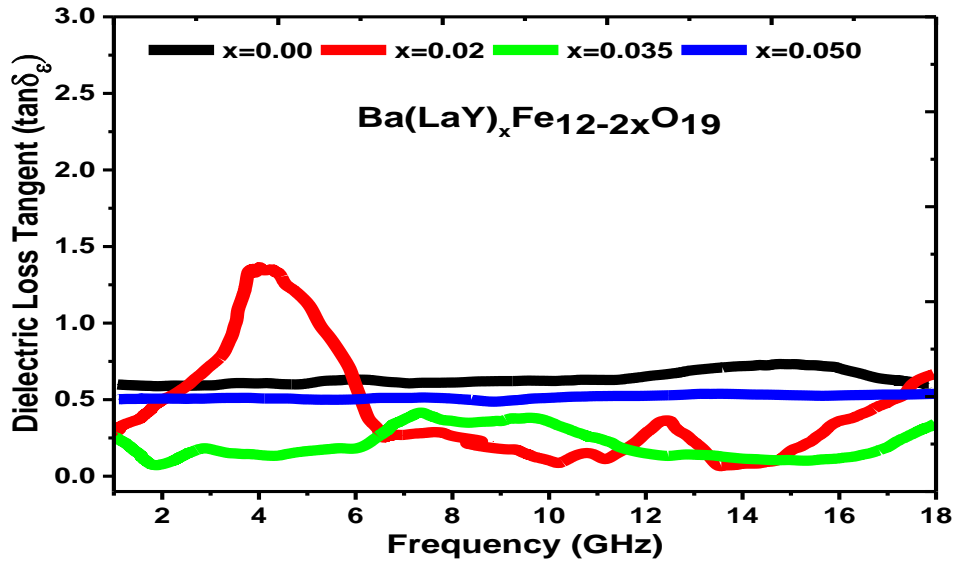


Figure 4.7: Dielectric loss tangent ($\tan\delta_\epsilon$) of La-Y substituted Barium hexaferrite nanoparticles.

4.5.3 Magnetic Loss Tangent

Figure 4.8 depicts the magnetic loss tangent ($\tan\delta_\mu$), which is the ratio of the imaginary part to the real part of permeability ($\tan\delta_\mu = \mu''/\mu'$). This ratio measures the efficiency of magnetic energy storage relative to the energy lost as heat. In this graph, the green curve ($x=0.035$) shows a large peak at around 6 GHz, indicating that the material at this doping level suffers from high magnetic losses in this frequency range, making it inefficient for applications requiring maximum energy dissipation. The black curve ($x=0.00$) again shows the lowest loss tangent, suggesting that the undoped material is more effective at storing magnetic energy with minimal losses.

The red and blue curves, corresponding to $x=0.020$ and $x=0.050$, show moderate losses with some fluctuations, but they generally remain lower than the green curve. This suggests that while doping can introduce additional magnetic losses, the effect is highly dependent on both the doping level and the frequency. Thus, careful selection of the doping level can optimize the material's performance for specific applications where low magnetic

losses are critical, particularly at higher frequencies where energy dissipation becomes more pronounced.

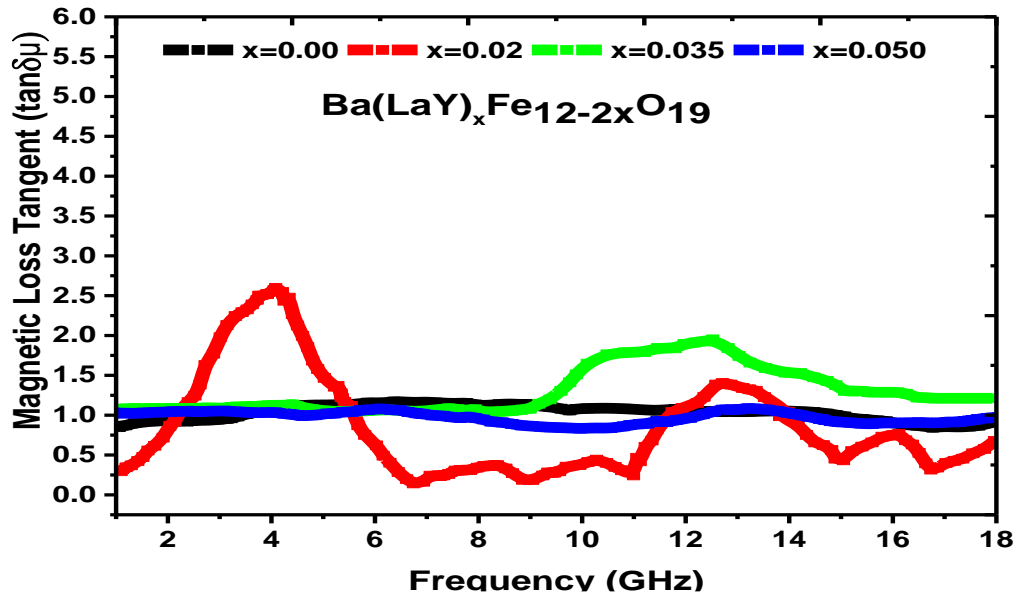


Figure 4.8: Magnetic loss tangent ($\tan\delta\mu$) of La-Y substituted Barium hexaferrite nanoparticles.

4.5.4 Impedance Matching and Reflection Loss

In many areas of electromagnetic theory and applications, impedance matching is a crucial idea, especially when trying to transfer as much power as possible between two media, like an electromagnetic wave and an absorbing substance. Impedance matching is a key idea in lowering reflection and improving a material's ability to absorb electromagnetic energy. This is especially crucial for designing absorbers for use in antennas, different microwave components, and radar-absorbing materials (RAM).

The impedance of a material's surface, often referred to as the input impedance Z_{in} , must closely match the impedance of the medium from which the wave is incident—typically free space in order to produce low reflection of incident electromagnetic waves. Free space impedance, represented by the symbol Z_0 , is roughly 377 ohms. For perfect impedance matching, the ratio of the absorber Z_{in} 's input impedance to the free space Z_0 's impedance should ideally equal 1. In order to maximize energy transfer, this condition

guarantees that all incident electromagnetic energy is absorbed by the medium without any reflection.

$$\text{Perfect Impedance matching} = Z_{\text{in}}/Z_0 = 1 \quad (4.5)$$

In this equation:

- Z_{in} represents the input impedance of the absorbing material.
- Z_0 is the characteristic impedance of free space, approximately equal to 377 ohms.

There is no impedance discontinuity at the contact when this ratio is equal to 1, which denotes that the material's impedance exactly matches that of empty space. Consequently, the electromagnetic wave is completely absorbed by the material and experiences no reflection at the boundary. In the design of many electromagnetic devices, where minimizing and regulating reflection is essential, this principle is applied.

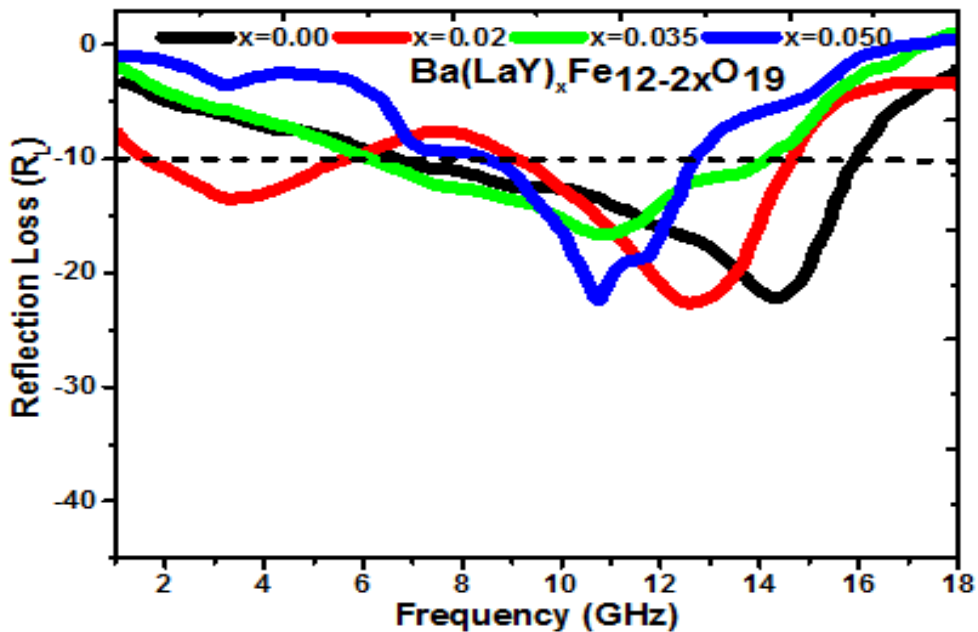


Figure 4.9: Frequency dependent of reflection loss (RL) of $\text{BaLa}_x\text{Y}_x\text{Fe}_{12-2x}\text{O}_{19}$ ($0.00 \leq x \leq 0.050$) with coating thickness of 2.45 mm in Ku band.

In transmission line theory, the performance of an absorbing material, particularly one backed by a metal layer, is assessed using two key parameters: reflection loss (RL) and input impedance. Reflection loss measures how much electromagnetic energy is reflected back from the material's surface, with lower reflection loss indicating better absorption. The goal is to minimize reflection loss, which happens when the impedance of the absorbing material matches the impedance of free space (377 ohms). This matching ensures that the material absorbs more of the incoming electromagnetic energy rather than reflecting it.

The input impedance of the material is crucial in this process. It is influenced by the thickness of the absorbing layer and its interaction with the metal backing. For an absorber backed by metal, the impedance needs to be adjusted to ensure it closely matches the impedance of free space. By carefully designing the thickness of the layer and considering its material properties, the impedance can be tuned to achieve optimal absorption and minimal reflection. This approach is essential in applications where controlling the reflection of electromagnetic waves is critical, such as in radar-absorbing materials and electromagnetic interference shielding.

Table 4.5: Impedance Matching and Reflection Loss

S.No	Sample	Max R_L (dB)	(RL) Peak Frequency (GHz)	Frequency band $RL < -10dB$ (GHz)	Bandwidth $RL < -10dB$ (GHz)
1.	0.00	-22.32	14.35	6.76 – 14.97	8.21
2.	0.020	-23.75	12.64	9.06 – 14.68	5.62
3.	0.035	-15.74	10.69	6.18 – 14.11	7.93
4.	0.050	-22.74	10.84	8.53 – 12.71	4.18

Figure 4.8 illustrates the reflection loss (R_L) of a material with the formula $BaLa_xY_xFe_{12-2x}O_{19}$ as a function of frequency, ranging from 2 GHz to 18 GHz. The reflection loss, measured in decibels (dB) shown on vertical axis of graph, indicates how effectively the material absorbs electromagnetic waves, with more negative values representing greater absorption.

The vertical axis measures the reflection loss in decibels (dB). Reflection loss quantifies how much of the incident electromagnetic wave energy is absorbed by the material rather than being reflected. A more negative R_L value indicates better absorption capability. For instance, an R_L value of -10 dB means that 90% of the incident energy is absorbed, while -20 dB indicates 99% absorption. The various colored curves (black, red, blue, and green) show variations in the material's composition and correlate to different values of x (0.00, 0.020, 0.035, and 0.05).

The material's capacity to absorb electromagnetic waves at various frequencies is affected by changes in its dielectric and magnetic characteristics. Every composition has a different reflection loss profile, as the graph demonstrates, with some frequencies corresponding to deeper troughs and best absorption at particular locations. For instance, a composition that is particularly good at absorbing electromagnetic waves at a given frequency is shown by a curve that dips more steeply at that frequency. This makes the composition perfect for applications that need focused frequency absorption.

By comparing the curves, it is clear that changing the value of x can improve the material's absorption properties. The capacity to tailor material characteristics to particular frequency ranges is essential for uses like microwave absorption, stealth technology, and shielding against electromagnetic interference (EMI).

For example, in order to prevent interference with electronic devices, materials used for EMI shielding must effectively absorb electromagnetic radiation. Choosing the right composition can improve performance over the intended frequency range. Materials that can absorb radar emissions at particular frequencies help with stealth technology by making an object harder to detect. The graph is a useful tool for comprehending the relationship between composition and electromagnetic absorption. It also offers

information on how to build materials specifically for technological uses. Researchers can determine the best material compositions for a variety of real-world applications by examining the reflection loss at various frequencies. This ensures that the material functions as best it can in its intended setting.

CHAPTER 5: CONCLUSIONS AND FUTURE RECOMMENDATION

5.1 Conclusion

Over the past 20 years, hexaferrites have been extensively referenced in literature regarding its application in recent technology. A fundamental prerequisite of these technologies is absolute control over the microstructure which includes control over the desired form and size of the particles for microwave absorption applications.

By using the sol-gel auto combustion approach, single phase La-Y substituted $\text{BaFe}_{12}\text{O}_{19}$ nanoparticles were produced which was confirmed by XRD analysis. The c/a ratio (value close to 3.807) from the XRD data supports the development of the magneto-plumbite hexagonal structure across all compositions. Substituting $\text{BaFe}_{12}\text{O}_{19}$ with La^{+3} (1.03 Å) and Y^{+3} (0.90 Å) ions, which have larger ionic radii compared to Fe^{+3} (0.64 Å), leads to an expansion of the lattice parameters and unit cell volume as the dopant concentration increases up to $x=0.050$. This substitution resulted in an increase in the average crystallite size (D_c), ranging from 39 to 45 nm with increasing dopant concentration up to $x=0.050$.

The doped compositions have lower values of saturation magnetization (M_s) and remanence (M_r) as compared to the undoped sample. The minimum values of M_s (40.89 emu/g) and M_r (4990 emu/g) were observed at $x=0.050$ while maximum values K_1 (118387.5 erg/cm³) was observed at $x=0.020$ indicating reflection loss shift towards lower frequency.

The reflection loss (RL) in the X-band (8 – 12 GHz) and Ku-band (12 – 18 GHz) was analyzed, revealing a maximum reflection loss of -23.75dB at $x=0.020$ with a bandwidth of 5.62 GHz. 90% of the incident energy is absorbed for $x=0.035$ while 99% absorption has been given by $x=0.050$. These results suggest that La-Y substituted barium hexaferrite is a promising candidate for microwave absorption materials (MAMs) with enhanced absorption properties. The microwave absorption capabilities of $\text{BaFe}_{12}\text{O}_{19}$ improve significantly upon substitution with La and Y, particularly at the optimal

concentration of $x=0.020$, making it the most effective composition for potential applications in electromagnetic interference (EMI) shielding and radar absorbing materials.

5.2 Future Recommendation

- Other rare earth metals combinations with transition metals can be used to further improve the microwave absorbing properties in X and Ku band. These ferrite powders can further be used to prepare polymer sheets of different thickness which can be tested at the entire frequency range of electromagnetic waves.
- Microwave absorption can be greatly increased by incorporating hexaferrite materials into hybrid systems or composite structures such as when they are combined with conductive polymers and carbon nanotubes. This development expands the range of possible uses, enhancing performance in fields like electromagnetic interference shielding and stealth technology to the advantage of both the military and civilian sectors.

REFERENCES

- [1] D.K. Cheng, Fundamentals of engineering electromagnetics, (1993).
- [2] E.F. Knott, J.F. Schaeffer, M.T. Tulley, Radar cross section, SciTech Publishing, 2004.
- [3] S. Sugimoto, K. Okayama, S.-i. Kondo, H. Ota, M. Kimura, Y. Yoshida, H. Nakamura, D. Book, T. Kagotani, M. Homma, Barium M-type ferrite as an electromagnetic microwave absorber in the GHz range, Mater. Trans., JIM, 39 (1998) 1080-1083.
- [4] S. Geetha, K. Sathesh Kumar, C.R. Rao, M. Vijayan, D. Trivedi, EMI shielding: Methods and materials—A review, J. Appl. Polym. Sci., 112 (2009) 2073-2086.
- [5] S. Trolier-McKinstry, R.E. Newnham, Materials engineering: bonding, structure, and structure-property relationships, Cambridge University Press, 2018.
- [6] J. Zhu, H. Gu, Z. Luo, N. Haldolaarachige, D.P. Young, S. Wei, Z. Guo, Carbon nanostructure-derived polyaniline metacomposites: electrical, dielectric, and giant magnetoresistive properties, Langmuir, 28 (2012) 10246-10255.
- [7] D. Jiang, V. Murugadoss, Y. Wang, J. Lin, T. Ding, Z. Wang, Q. Shao, C. Wang, H. Liu, N. Lu, Electromagnetic interference shielding polymers and nanocomposites-a review, Polymer Reviews, 59 (2019) 280-337.
- [8] C. Cheng, R. Fan, Z. Wang, Q. Shao, X. Guo, P. Xie, Y. Yin, Y. Zhang, L. An, Y. Lei, Tunable and weakly negative permittivity in carbon/silicon nitride composites with different carbonizing temperatures, Carbon, 125 (2017) 103-112.
- [9] L. Nicolaescu, T. Oroian, Radar cross section, in: 5th International Conference on Telecommunications in Modern Satellite, Cable and Broadcasting Service. TELSIKS 2001. Proceedings of Papers (Cat. No. 01EX517), IEEE, 2001, pp. 65-68.
- [10] Y. Lee, E. Kim, Y. Park, J. Kim, W. Ryu, J. Rho, K. Kim, Photodeposited metal-semiconductor nanocomposites and their applications, Journal of Materiomics, 4 (2018) 83-94.
- [11] W. Shen, T. Ou, J. Wang, T. Qin, G. Zhang, X. Zhang, Y. Han, Y. Ma, C. Gao, Effects of high pressure on the electrical resistivity and dielectric properties of nanocrystalline SnO₂, Scientific reports, 8 (2018) 1-10.
- [12] L. Wang, Q. Di, M. Sun, J. Liu, C. Cao, J. Liu, M. Xu, J. Zhang, Assembly-promoted photocatalysis: Three-dimensional assembly of CdS_xSe_{1-x} (x= 0–1) quantum dots into nanospheres with enhanced photocatalytic performance, Journal of Materiomics, 3 (2017) 63-70.

- [13] J. Li, X. Zhang, B. Duan, Y. Cui, H. Yang, H. Wang, J. Li, X. Hu, G. Chen, P. Zhai, Pressure induced convergence of conduction bands in Al doped Mg₂Si: Experiment and theory, *Journal of Materiomics*, 5 (2019) 81-87.
- [14] Z. Zhang, Z. Cai, Y. Zhang, Y. Peng, Z. Wang, L. Xia, S. Ma, Z. Yin, R. Wang, Y. Cao, The recent progress of MXene-Based microwave absorption materials, *Carbon*, 174 (2021) 484-499.
- [15] M. Dahl, Y. Liu, Y. Yin, Composite titanium dioxide nanomaterials, *Chem. Rev.*, 114 (2014) 9853-9889.
- [16] B.R. Smith, S.S. Gambhir, Nanomaterials for in vivo imaging, *Chem. Rev.*, 117 (2017) 901-986.
- [17] G. Aragay, F. Pino, A. Merkoci, Nanomaterials for sensing and destroying pesticides, *Chem. Rev.*, 112 (2012) 5317-5338.
- [18] X. Yang, M. Yang, B. Pang, M. Vara, Y. Xia, Gold nanomaterials at work in biomedicine, *Chem. Rev.*, 115 (2015) 10410-10488.
- [19] J. Bai, B. Zhou, Titanium dioxide nanomaterials for sensor applications, *Chem. Rev.*, 114 (2014) 10131-10176.
- [20] L. Jing, S.V. Kershaw, Y. Li, X. Huang, Y. Li, A.L. Rogach, M. Gao, Aqueous based semiconductor nanocrystals, *Chem. Rev.*, 116 (2016) 10623-10730.
- [21] L. Guan, X. Chen, Photoexcited charge transport and accumulation in anatase TiO₂, *ACS Applied Energy Materials*, 1 (2018) 4313-4320.
- [22] X. Chen, L. Liu, P.Y. Yu, S.S. Mao, Increasing solar absorption for photocatalysis with black hydrogenated titanium dioxide nanocrystals, *Science*, 331 (2011) 746-750.
- [23] X. Chen, C. Li, M. Grätzel, R. Kostecki, S.S. Mao, Nanomaterials for renewable energy production and storage, *Chem. Soc. Rev.*, 41 (2012) 7909-7937.
- [24] C. Burda, X. Chen, R. Narayanan, M.A. El-Sayed, Chemistry and properties of nanocrystals of different shapes, *Chem. Rev.*, 105 (2005) 1025-1102.
- [25] X.C. Tong, *Advanced materials and design for electromagnetic interference shielding*, CRC press, 2016.
- [26] D.M. Pozar, *Microwave engineering*, Fourth Editions, University of Massachusetts at Amherst, John Wiley & Sons, Inc, (2012) 26-30.
- [27] M. Green, X. Chen, Recent progress of nanomaterials for microwave absorption, *Journal of Materiomics*, 5 (2019) 503-541.

- [28] A. Kumar, V. Agarwala, D. Singh, Effect of milling on dielectric and microwave absorption properties of SiC based composites, *Ceram. Int.*, 40 (2014) 1797-1806.
- [29] P. Wang, X. Wang, L. Qiao, J. Zhang, G. Wang, B. Duan, T. Wang, F. Li, High-frequency magnetic properties and microwave absorption performance of oxidized Pr₂Co₁₇ flakes/epoxy composite in x-band, *J. Magn. Magn. Mater.*, 468 (2018) 193-199.
- [30] M. Duan, L. Yu, L. Sheng, K. An, W. Ren, X. Zhao, Electromagnetic and microwave absorbing properties of SmCo coated single-wall carbon nanotubes/NiZn-ferrite nanocrystalline composite, *J. Appl. Phys.*, 115 (2014) 174101.
- [31] B.-W. Li, Y. Shen, Z.-X. Yue, C.-W. Nan, Enhanced microwave absorption in nickel/hexagonal-ferrite/polymer composites, *Appl. Phys. Lett.*, 89 (2006) 132504.
- [32] Y. Feng, C. Tang, T. Qiu, Effect of ball milling and moderate surface oxidization on the microwave absorption properties of FeSiAl composites, *Materials Science and Engineering: B*, 178 (2013) 1005-1011.
- [33] T. Gong, P. Li, Q. Sui, L.-J. Zhou, N.-N. Yang, E.-Q. Gao, Switchable Ferro-, Ferri-, and Antiferromagnetic States in a Piezo- and Hydrochromic Metal–Organic Framework, *Inorg. Chem.*, 57 (2018) 6791-6794.
- [34] X. Ren, H. Fan, Y. Cheng, Microwave absorption properties of double-layer absorber based on carbonyl iron/barium hexaferrite composites, *Appl. Phys. A*, 122 (2016) 1-7.
- [35] Y. Naito, K. Suetake, Application of ferrite to electromagnetic wave absorber and its characteristics, *IEEE Transactions on Microwave Theory and Techniques*, 19 (1971) 65-72.
- [36] K.J. Vinoy, R.M. Jha, Radar absorbing materials: from theory to design and characterization, (1996).
- [37] K. Matsuta, T. Minamisono, M. Tanigaki, M. Fukuda, Y. Nojiri, M. Mihara, T. Onishi, T. Yamaguchi, A. Harada, M. Sasaki, Magnetic moments of proton drip-line nuclei ¹³O and ⁹C, *Hyperfine Interact.*, 97 (1996) 519-526.
- [38] G. Viau, F. Ravel, O. Acher, F. Fiévet-Vincent, F. Fiévet, Preparation and microwave characterization of spherical and monodisperse Co₂₀Ni₈₀ particles, *J. Appl. Phys.*, 76 (1994) 6570-6572.
- [39] L. Olmedo, G. Chateau, C. Deleuze, J. Forveille, Microwave characterization and modelization of magnetic granular materials, *J. Appl. Phys.*, 73 (1993) 6992-6994.
- [40] H.K. Choudhary, R. Kumar, S.P. Pawar, S. Bose, B. Sahoo, Effect of microstructure and magnetic properties of Ba-Pb-hexaferrite particles on EMI shielding behavior of Ba-Pb-hexaferrite-polyaniline-wax nanocomposites, *J. Electron. Mater.*, 49 (2020) 1618-1629.

- [41] J.D. Adam, L.E. Davis, G.F. Dionne, E.F. Schloemann, S.N. Stitzer, Ferrite devices and materials, *IEEE transactions on microwave theory and techniques*, 50 (2002) 721-737.
- [42] R. Mudsainiyan, S. Chawla, S. Meena, Correlation between site preference and magnetic properties of Co–Zr doped BaCo_xZr_xFe_(12–2x)O₁₉ prepared under sol–gel and citrate precursor sol–gel conditions, *J. Alloys Compd.*, 615 (2014) 875-881.
- [43] S. Trukhanov, A. Trukhanov, V. Kostishin, L. Panina, I. Kazakevich, V. Turchenko, V. Kochervinskii, Coexistence of spontaneous polarization and magnetization in substituted M-type hexaferrites BaFe_{12–x}Al_xO₁₉ ($x \leq 1.2$) at room temperature, *JETP letters*, 103 (2016) 100-105.
- [44] H. Kojima, Fundamental properties of hexagonal ferrites with magnetoplumbite structure, *Handbook of ferromagnetic materials*, 3 (1982) 305-391.
- [45] I. Orlov, L. Palatinus, A. Arakcheeva, G. Chapuis, Hexagonal ferrites: a unified model of the (TS) nT series in superspace, *Acta Crystallogr. Sect. B: Struct. Sci.*, 63 (2007) 703-712.
- [46] R. Peymanfar, A. Mohammadi, S. Javanshir, Preparation of graphite-like carbon nitride/polythiophene nanocomposite and investigation of its optical and microwave absorbing characteristics, *Composites Communications*, 21 (2020) 100421.
- [47] H. Sözeri, H. Deligöz, H. Kavas, A. Baykal, Magnetic, dielectric and microwave properties of M–Ti substituted barium hexaferrites (M= Mn²⁺, Co²⁺, Cu²⁺, Ni²⁺, Zn²⁺), *Ceram. Int.*, 40 (2014) 8645-8657.
- [48] S. Iqbal, J. Shah, R. Kotnala, S. Ahmad, Highly efficient low cost EMI shielding by barium ferrite encapsulated polythiophene nanocomposite, *J. Alloys Compd.*, 779 (2019) 487-496.
- [49] A. Zafar, A. ur Rahman, S. Shahzada, S. Anwar, M. Khan, A. Nisar, M. Ahmad, S. Karim, Electrical and magnetic properties of nano-sized Eu doped barium hexaferrites, *J. Alloys Compd.*, 727 (2017) 683-690.
- [50] S.B. Narang, C. Singh, Y. Bai, I. Hudiara, Microstructure, hysteresis and microwave absorption analysis of Ba (1– x) Sr_xFe₁₂O₁₉ ferrite, *Mater. Chem. Phys.*, 111 (2008) 225-231.
- [51] P. Bhattacharya, C.K. Das, In situ synthesis and characterization of CuFe₁₀Al₂O₁₉/MWCNT nanocomposites for supercapacitor and microwave-absorbing applications, *Industrial & Engineering Chemistry Research*, 52 (2013) 9594-9606.
- [52] R. Ji, M. Yang, J. Lv, Z. Wang, Y. Shi, X. Song, A. Xie, J. Liu, M. Zhang, Carboxylation-induced polyaniline morphology on surfaces of barium hexaferrite nano

particles with enhanced microwave absorbing properties, *J. Alloys Compd.*, 883 (2021) 160839.

[53] F. Xu, L. Ma, M. Gan, J. Tang, Z. Li, J. Zheng, J. Zhang, S. Xie, H. Yin, X. Shen, Preparation and characterization of chiral polyaniline/barium hexaferrite composite with enhanced microwave absorbing properties, *J. Alloys Compd.*, 593 (2014) 24-29.

[54] H. Qiu, X. Luo, J. Wang, X. Zhong, S. Qi, Synthesis and characterization of ternary polyaniline/barium ferrite/reduced graphene oxide composite as microwave-absorbing material, *J. Electron. Mater.*, 48 (2019) 4400-4408.

[55] L. Du, Y. Du, Y. Li, J. Wang, C. Wang, X. Wang, P. Xu, X. Han, Surfactant-assisted solvothermal synthesis of Ba (CoTi) x Fe_{12-2x}O₁₉ nanoparticles and enhancement in microwave absorption properties of polyaniline, *The Journal of Physical Chemistry C*, 114 (2010) 19600-19606.